

# IDEA League

MASTER OF SCIENCE IN APPLIED GEOPHYSICS

RESEARCH THESIS

---

Image data filtering and automatic detection of damages within asphalt with the help of ground-penetrating radar (GPR) and machine learning methods

Zifan Zhang

---

July 2022



**Image data filtering and automatic detection of  
damages within asphalt with the help of  
ground-penetrating radar (GPR) and machine  
learning methods**

MASTER OF SCIENCE THESIS

for the degree of Master of Science in Applied Geophysics

by

Zifan Zhang

July 2022

IDEA LEAGUE  
JOINT MASTER IN APPLIED GEOPHYSICS

TU Delft, the Netherlands  
ETH Zürich, Switzerland  
RWTH Aachen, Germany

Dated: *July 2022*

---

Supervisors:

(main) Prof.dr.ir. E.C. Slob  
ing. R.H. van Beuningen

# Abstract

Damages within asphalt have been interesting phenomena in asphalt engineering, the detection of which is significant for maintenance of road sections. This project focuses on cracks and delaminations. An attempt was made to filter radar image data with a method based on a VNA-antenna-multilayered system model as well as the data from two specific measurements, aiming at better visualizing cracks as well as other features in radar image, and the results were checked and analysed. This part of work has provided an application of the aforementioned method of radar image data filtering as well as the points worth noticing and avoiding when making this application. For delaminations, machine learning algorithms, first the EM algorithm and then the YOLO v3 algorithm, were used as an attempt to highlight and detect them. Though the results still need improving, it is still valuable that the workload for human intervention can be alleviated with the help of these algorithms and that better performance can be expected based on current work, with the increasing amount of data with high quality achieved in the future.

# Acknowledgements

Many thanks for the precious advice and guidance of Prof.dr.ir. E.C. Slob, my supervisor in TU Delft, and ing. R.H. van Beuningen, my supervisor in Heijmans.

The framework of the programme realizing the EM algorithm was based on the code in Exercise 1 of the 'Machine Learning' course in semester WS 2021 of RWTH Aachen, by Prof. Dr. Bastian Leibe, M.Sc. George Lydakis and M.Sc. Idil Esen Zulfikar. I modified the original code and then applied it to my own problem.

Regarding the programme as an application of the YOLO v3 algorithm, I used the open source code by Muehleemann:

<https://github.com/AntonMu/TrainYourOwnYOLO>

I also referred to his tutorial 'How to train your own YOLOv3 detector from scratch' published in Insight:

<https://blog.insightdatascience.com/how-to-train-your-own-yolov3-detector-from-scratch-224d10e55de2>

The YOLO v3 algorithm itself was developed by Redmon et al. [15], with the relevant aspects accessible from:

<https://pjreddie.com/darknet/yolo/>

Based on the model with pretrained weights, I trained the network and also tested it with my own datasets.

The first fieldwork at the Lekdijk for the crack data as well as the sky-shot and the metal plate measurements in Rosmalen for the filters part were conducted by R.H. van Beuningen and me.

For the second fieldwork for the delamination data, A1AT was measured from the end of March to the beginning of May in 2022 while the older project A1AA which was also used was measured in September and November of 2018, by my colleague ing. H. van der Linden and some other colleagues from the Geophysical department in Heijmans. The visual inspection at the Lekdijk was conducted by H. van der Linden and another colleague ing. Y. Blom.

Regarding the empirical values and settings most often applied in asphalt engineering for the filters in the Examiner software, I discussed them with my colleague ing. M.C. Bosma, who is experienced in these aspects.

Also many thanks for all colleagues who have made efforts to this thesis project.

# Contents

<b>1</b>	<b>Introduction</b>	<b>10</b>
1.1	Damage types . . . . .	10
1.2	Project goals . . . . .	10
1.3	Project sites . . . . .	10
1.4	Measurement devices and software . . . . .	12
1.4.1	Measurement devices . . . . .	12
1.4.2	Measurement software . . . . .	14
<b>2</b>	<b>Measurements and data processing in Examiner</b>	<b>16</b>
2.1	Measurements . . . . .	16
2.1.1	Measurement settings . . . . .	16
2.1.2	View in 3D - Examiner . . . . .	16
2.2	Data processing software, inbuilt filters and settings . . . . .	17
2.2.1	General aspects, inbuilt filters and parameters . . . . .	17
2.2.2	The Road Template . . . . .	19
2.2.3	Interference suppression . . . . .	19
2.2.4	IFFT/ISDFT . . . . .	21
2.2.5	Background removal filter . . . . .	21
2.2.6	Summary of inbuilt filters . . . . .	22
<b>3</b>	<b>Filters</b>	<b>24</b>
3.1	The way of filtering . . . . .	24
3.2	The model system . . . . .	25
3.3	Filters and the Green's function . . . . .	26
3.3.1	Impulse response calculation . . . . .	26
3.3.2	The matrix system . . . . .	26
3.3.3	The Green's function for specific cases . . . . .	27
3.4	Assumptions . . . . .	28
3.5	The sky-shot and the metal plate measurements . . . . .	28
3.5.1	Sky-shot measurement . . . . .	28
3.5.2	Metal plate measurement . . . . .	29
3.6	Measurement data processing . . . . .	30
3.6.1	Channel average and trace average . . . . .	30

3.6.2	Time domain data at different heights . . . . .	31
3.6.3	Frequency domain spectrum . . . . .	33
3.7	Checking the solution . . . . .	35
3.7.1	Robustness check . . . . .	35
3.7.2	Bias check . . . . .	35
3.7.3	Pattern check . . . . .	36
3.8	Discussion and analysis on the results . . . . .	37
<b>4</b>	<b>Application of machine learning methods</b>	<b>38</b>
4.1	Expectation maximization . . . . .	38
4.1.1	Principle . . . . .	38
4.1.2	Selection of training data and parameter . . . . .	39
4.2	Classification and object detection . . . . .	43
4.2.1	Principles . . . . .	43
4.2.2	Classification of delamination . . . . .	44
4.2.3	My datasets: training, validation and testing . . . . .	46
4.2.4	Testing results . . . . .	46
4.3	Summary and discussion . . . . .	49
<b>5</b>	<b>Conclusions and future work</b>	<b>50</b>
<b>A</b>	<b>The Green's function of a metal plate</b>	<b>53</b>
<b>B</b>	<b>Explanation on the choice of data set for object detection</b>	<b>55</b>

# List of Figures

1.1	The two sites for data acquisition . . . . .	11
1.2	Lekdijk drill core sample 392 . . . . .	11
1.3	Visual inspection . . . . .	12
1.4	Overview of measurement devices . . . . .	12
1.5	Batteries inside the vehicle to power the measurement system . . . . .	13
1.6	3D - Radar DX2125 antenna array coupled with the front of vehicle . . . . .	13
1.7	The GPS coupled with the vehicle . . . . .	14
1.8	The DMI . . . . .	14
1.9	The Geoscope software . . . . .	15
2.1	Location 1 and Location 2 at the Lekdijk site . . . . .	17
2.2	General aspects of data processing . . . . .	17
2.3	The gain function . . . . .	18
2.4	Interference suppression with power limit value . . . . .	20
2.5	Interference suppression of the deeper subsurface with power limit value . . . . .	20
2.6	Background removal filter with the window type . . . . .	22
2.7	Background removal filter . . . . .	22
3.1	Multilayered medium with point source . . . . .	25
3.2	The linear system model in series and parallel of the VNA-antenna-multilayered multilayered system . . . . .	25
3.3	The sky-shot measurement . . . . .	29
3.4	The metal plate measurement . . . . .	29
3.5	Antenna dimensions and directions . . . . .	30
3.6	Examples of t-x domain measurement data profile . . . . .	31
3.7	Time domain metal plate data at various heights . . . . .	32
3.8	Time domain metal plate data at various heights by Lambot et al. . . . .	32
3.9	Time domain Green's function value at various heights . . . . .	33
3.10	Time domain Green's function value at various heights by Lambot et al. . . . .	33
3.11	f-x domain spectrum of the two measurement data . . . . .	34
3.12	f-x domain spectrum of S11 . . . . .	34
3.13	The robustness check . . . . .	35
3.14	The bias check . . . . .	36
3.15	Pattern check . . . . .	36

3.16	Pattern check: patterns of the filters in previous work . . . . .	37
4.1	The training figure (A1L267, magnitude, jet) . . . . .	40
4.2	The result of feature detection . . . . .	41
4.3	The result of feature detection (real) . . . . .	42
4.4	Darknet-53 architecture . . . . .	43
4.5	YOLO v3 network architecture . . . . .	44
4.6	Examples of Type 1 delamination . . . . .	44
4.7	Examples of Type 2 delamination . . . . .	45
4.8	Examples of Type 3 delamination . . . . .	45
4.9	Results of detection on the testing set from A1AT (12 out of 108 images)	47
4.10	Results of detection on the testing set from A1AT (with more than one type) . . . . .	48
4.11	Results of detection on the testing set from A1AA . . . . .	49
5.1	Examples of radar image from the demo project . . . . .	51

# List of Tables

2.1	Measurement settings . . . . .	16
2.2	Filters for radar data in Examiner 3.5.0 . . . . .	18
2.3	Filters and default values of the main parameters in road template . . .	19

# Chapter 1

## Introduction

### 1.1 Damage types

There are many kinds of asphalt damages, and what asphalt engineers are most interested in includes voids, delaminations and cracks.

Voids are pores filled with air and/or water that appear in asphalt engineering projects, which are observed most often on the interface between the bottom asphalt layer and the foundation layer.

Delaminations in asphalt engineering mean the separation between different layers, which can be either the asphalt layer or the foundation layer, while what is focused on in this case is mainly delaminations between asphalt layers.

Cracks are the type of damage with the largest degree of variation in both structure and dimension, which can occur anywhere within asphalt layers.

### 1.2 Project goals

In this project, I focus on cracks and delaminations while voids are not of most interest. Based on the radar data from several project sites of Heijmans, my work mainly includes radar image data filtering as an attempt to better visualize the cracks in radar profiles as well as classifying and detecting the delaminations in radar profiles with machine learning algorithms.

### 1.3 Project sites

There are two sites where the field works were conducted for data acquisition:



(a) The Lekdijk site



(b) The A1 site

Figure 1.1: The two sites for data acquisition

The first one is the Lekdijk site, as is shown in Figure 1.1a<sup>1</sup>, mainly providing crack data. The drilled core samples, which is mentioned as drill core samples as a name commonly used by asphalt engineers, were not very helpful in this case since the really interesting cracks were only observed in one of the samples inspected. That was sample 392, where cracks appear in the top layer and stop, with the intact lower layers, as shown in Figure 1.2.

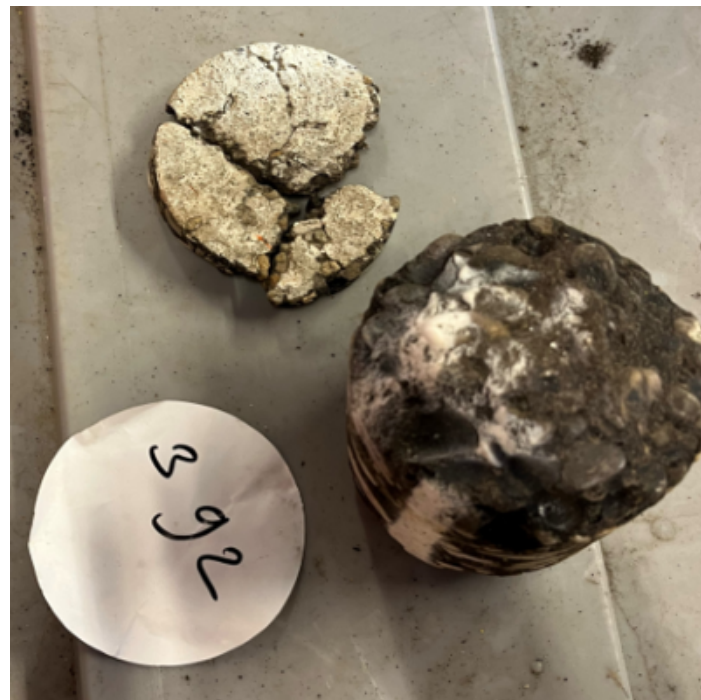


Figure 1.2: Lekdijk drill core sample 392

No visible cracks were observed in any other sample, and the probable explanation is that cracks exist in the volume around the samples but don't appear in the specific position where the samples were taken. Then the confirmation of the cracks at the Lekdijk site was mainly realized by the visual inspection.

<sup>1</sup>Figure 1.1a and 1.1b were provided by H. van der Linden.



(a) On road section



(b) In ArcGIS

Figure 1.3: Visual inspection

Although not much interesting information could be extracted from the drill core samples in this case, quite a few obvious cracks were confirmed by the detailed visual inspection, one example of which is shown in Figure 1.3a. The results of this inspection were visualized in ArcGIS, corresponding to the red annotations as shown in Figure 1.3b indicating these areas of interest for further inspection, and later in the Examiner software. For every crack in the visual inspection, there is also an available picture for it.

The second one is near Apeldoorn, including two projects A1AT (A1 Apeldoorn - Twello) and A1AA (A1 Apeldoorn - Azelo), as shown in Figure 1.1b, where many drill core samples were made for confirming the delaminations. In the A1AT project, almost all of the road sections were covered in the measurement while those in the A1AA project were only partially measured.

## 1.4 Measurement devices and software

### 1.4.1 Measurement devices

All of our measurement devices were coupled to the vehicle as shown in Figure 1.4a:



(a) The vehicle



(b) The Geoscope

Figure 1.4: Overview of measurement devices

and connected to the Geoscope device inside the vehicle as shown in Figure 1.4b, including connection to the Global Positioning System (GPS), the Distance Measuring Instrument (DMI), the antennas, the network as well as the power source respectively, as shown from left to right in order.

The measurement system was powered by the batteries in the carriage, as shown in Figure 1.5 as follows:

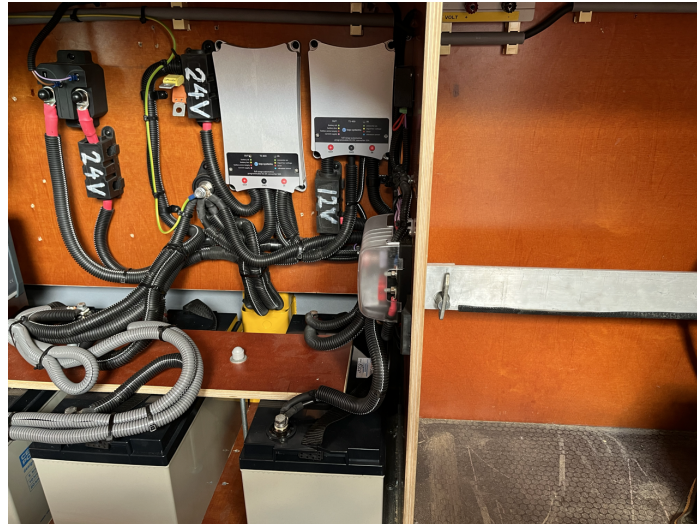


Figure 1.5: Batteries inside the vehicle to power the measurement system

The batteries were in the left part, while in the top-right part were the sockets for connection.

Our measurements for the subsurface were conducted with the 3D - Radar DX2125 antenna array, as shown in Figure 1.6.

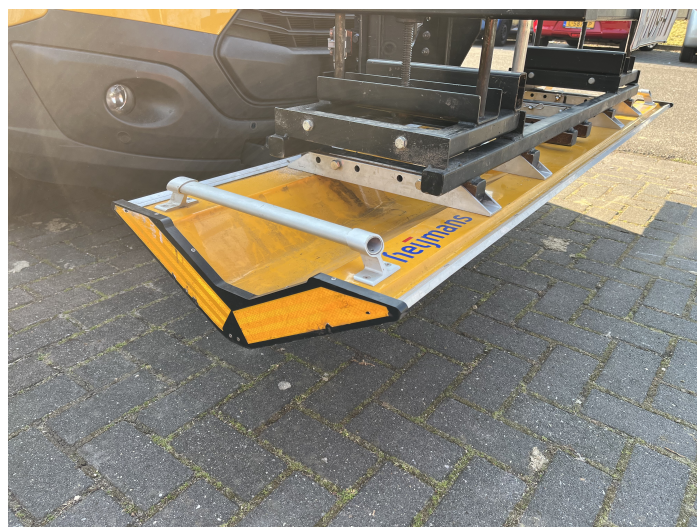


Figure 1.6: 3D - Radar DX2125 antenna array coupled with the front of vehicle

The antennas were air-coupled, fixed to the shelf coupled with the front of the vehicle and connected to the Geoscope in the carriage via a cable as mentioned above.

The Leica GS18 GPS was coupled to the top of the shelf, fixed by two bars, providing specific positioning data, as shown in Figure 1.7a and 1.7b.



(a) The GPS



(b) The GPS with close view

Figure 1.7: The GPS coupled with the vehicle

The DMI was coupled to the wheel hub for measuring the distances, and connected to the Geoscope in the carriage via a cable, as shown in Figure 1.8a and 1.8b respectively.



(a) Coupled with the wheel hub

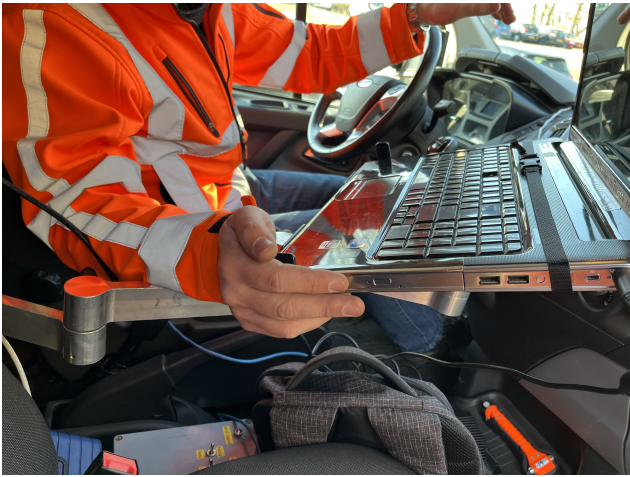


(b) Connected to the Geoscope in the carriage

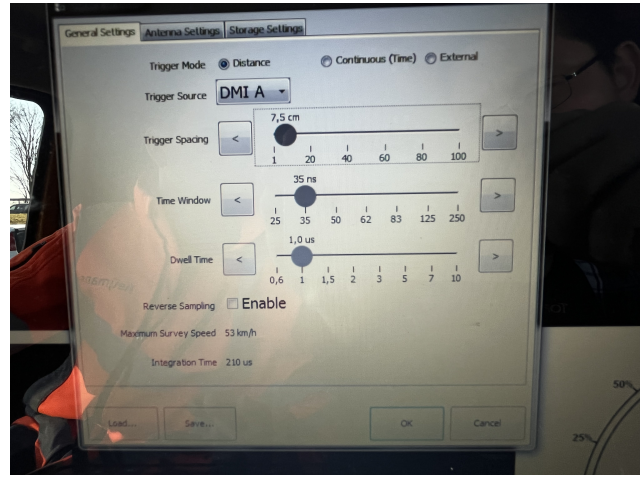
Figure 1.8: The DMI

#### 1.4.2 Measurement software

A laptop in the vehicle, as shown in Figure 1.9a, was used for recording and controlling the measurement with the Geoscope software, as shown in Figure 1.9b.



(a) The controlling laptop



(b) Setting the parameters of measurement in Geoscope

Figure 1.9: The Geoscope software

The measurement settings as well as the relevant parameters can be adjusted according to different measurement requirements, which is discussed in the following chapter.

# Chapter 2

## Measurements and data processing in Examiner

### 2.1 Measurements

#### 2.1.1 Measurement settings

The minimum frequency and the maximum frequency of the radar were fixed at 40.0 (MHz) and 2980.0 (MHz) respectively, while three different measurement settings were applied in our measurements, as shown in Table 1.1.

	<i>Setting 1</i>	<i>Setting 2</i>	<i>Setting 3</i>
Frequency step (MHz)	14.0	20.0	20.0
Time window (ns)	35	25	25
Dwell time ( $\mu$ s)	1.0	1.0	5.0
Sampling interval (mm)	74.8	20.2	74.8
maximum speed (km/h)	ca. 53	ca. 20	ca. 20

Table 2.1: Measurement settings

Setting 1, i.e. the normal setting, is the one with a speed which is acceptable in the efficiency of measurement and is also the most frequently applied one in real cases, while the second and the third settings are more detailed in measurement but with a lower speed.

All measurements can be viewed in the Examiner software, which is further discussed in the following section.

#### 2.1.2 View in 3D - Examiner

The two locations, Location 1 and Location 2, are shown in Figure 2.1, with a lot of cracks viewed specifically.

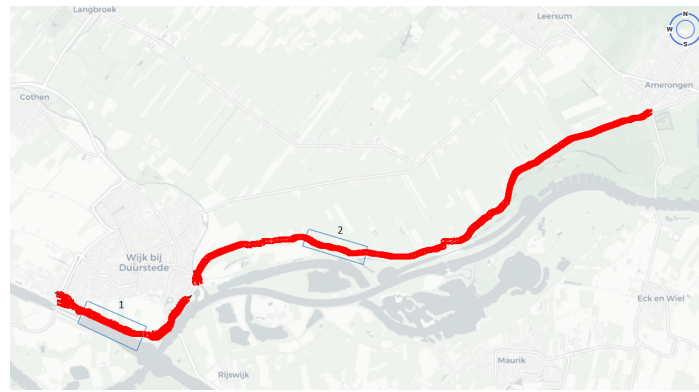


Figure 2.1: Location 1 and Location 2 at the Lekdijk site

The first two settings were applied to the measurements conducted within Location 1, while all of the three settings were used within Location 2. Only the normal setting was applied to the measurements conducted on the intermediate road sections between the two locations.

## 2.2 Data processing software, inbuilt filters and settings

### 2.2.1 General aspects, inbuilt filters and parameters

The Examiner 3.5.0 software<sup>1</sup> has been used to process the radar data. To begin with, I explored some parameters of the general aspects, as shown in Figure 2.2, before tuning the parameters of the filters.

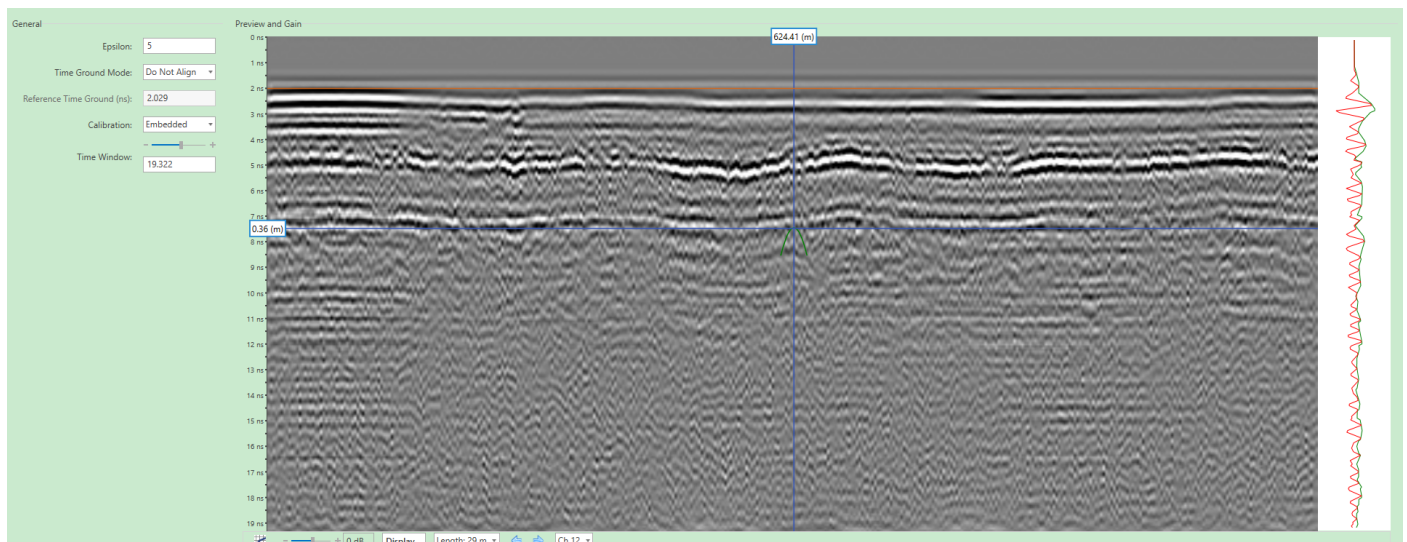


Figure 2.2: General aspects of data processing

All useful information for me is almost totally above the time window limit of 10 (ns) as I'm most interested in cracks and delaminations, most of which exist within the asphalt layers in the shallow subsurface, approximately with a thickness of 30-40 (cm)

<sup>1</sup>It is mentioned as 'Examiner' or some similar names for convenience.

in this case. Thus, I set the time window value as 10 (ns) as this would be sufficient for observing the effect of filtering on interesting parts.

The value of 5 for the dielectric constant is empirically adequate for asphalt. For the gain function, either keeping it as default<sup>2</sup>, as indicated by the dashed green line in Figure 2.3, or modifying it to give comparatively a bit stronger reinforcement to the shallower part, as indicated by the solid purple line in the same figure, is good enough empirically.

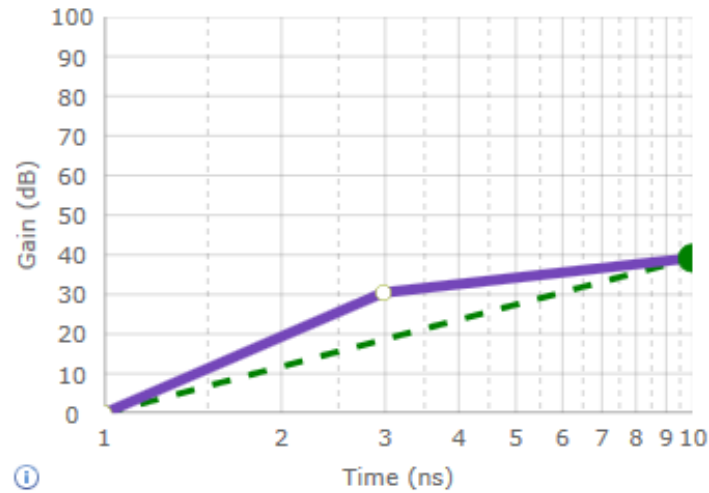


Figure 2.3: The gain function

All available filters in Examiner are shown in Table 2.2 below.

<i>Domain</i>	<i>Filter</i>
Frequency domain processing	Interference suppression
Frequency-to-time conversion	IFFT
	ISDFT
Time domain processing	Background removal filter
	Gradual low-pass filter
	Migration (Kirchhoff)
	Thick slices

Table 2.2: Filters for radar data in Examiner 3.5.0

Among all the filters, the key point of the gradual low-pass filter is to clean the data from noises and to reveal weak reflectors in deeper subsurface. Empirically, it’s usually used for targets like utilities, including pipes, cables, etc., often with larger depths than the targets in our case. Thus, this filter is not applied in the default data processing workflow of the road template, and the thick slices function is not needed in our case either.

Assuming that the inbuilt filters are independent from each other, i.e. the functions of different inbuilt filters do not have influence on each other, the effect of different filters together with parameter values were compared with each other while all of the other

<sup>2</sup>From now on, when a parameter, filter, setting, etc. is mentioned as default, it means the default counterpart in the ‘Road’ template of Examiner, which is further discussed in the next subsection.

conditions were kept as the same<sup>3</sup>. Before exploring the effect of any single filter, let's first have a look at the existing templates.

## 2.2.2 The Road Template

There are three existing templates in Examiner: 'Default', 'Utility Mapping' and 'Road' respectively, among which the 'Road' template, referred to as the road template from now on, is the most frequently used one for processing data relevant to asphalt layers in road sections. The filters, together with the default values of the main parameters, are shown in Table 2.3.

<i>Filter</i>	<i>Default main parameter</i>
Interference Suppression	Power Limit (dB): 16 Output Percentages: Enabled
IFFT	Window Type: Kaiser Kaiser Beta: 6
Background Removal Filter (the 1 <sup>st</sup> one)	Filter Length (m): 50 Removal (%): 100 Start Depth (ns): 4 Transition Zone (ns): 2 Filter Mode: Sliding window mean
Background Removal Filter (the 2 <sup>nd</sup> one)	Removal (%): 85 Start Depth (ns): 0 Transition Zone (ns): 0 Filter Mode: Mean

Table 2.3: Filters and default values of the main parameters in road template

The two background removals are in cascade. In the following subsections, each of these filters included in this template, which are the most important ones for asphalt engineers, are discussed.

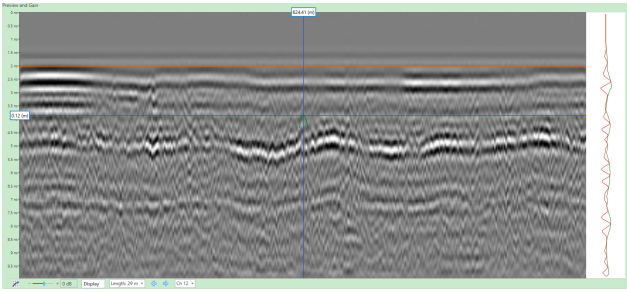
## 2.2.3 Interference suppression

The interference suppression filter removes the interference from external electromagnetic (EM) sources, where the parameter power limit (dB) controls the threshold (dB) for the suppression of potential interference. I adjusted the value, and made comparison between the results of an example with time window of 10 (ns), as shown in Figure 2.4a - 2.4d.

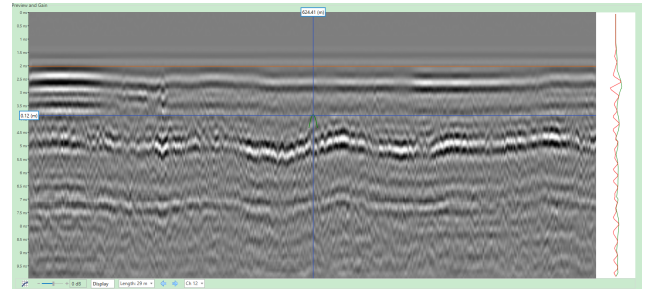
---

<sup>3</sup>For each comparison below, the other conditions, which were kept as the same, are not mentioned specifically here. It's not for the purpose of simplicity, but because:

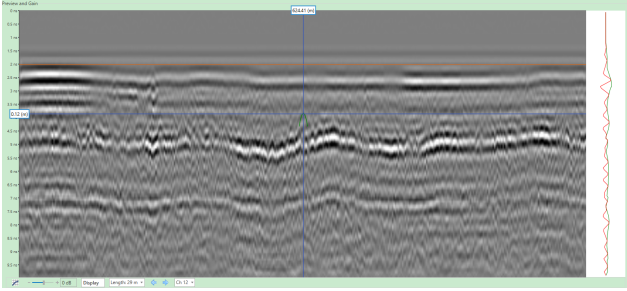
1. Under the assumption of independent filters as mentioned, the exact conditions of the other filters, while comparing the effect of a certain filter, are not important anymore, since they don't have any influence on the performance of the current filter which is being compared and thus have no influence on the result of comparison as well as the final choice of parameters, as long as they are kept as the same.
2. The comparisons were based on the 'Preview and Gain' section in the 'Region Processing Settings and Gain Settings' of a data region in Examiner. The way it works is that it displays a certain radar profile which the software selects from the data region that I selected. Before I made comparison with this function, I just randomly selected a data region, whose number I did not record, while the mechanism how the software selects the certain profile from this region for display after that is unknown for me. Thus, even if the other conditions were exactly listed, it would be hard to obtain the exactly same figures as what I have obtained as shown in this section since the final data to display would most probably be different.



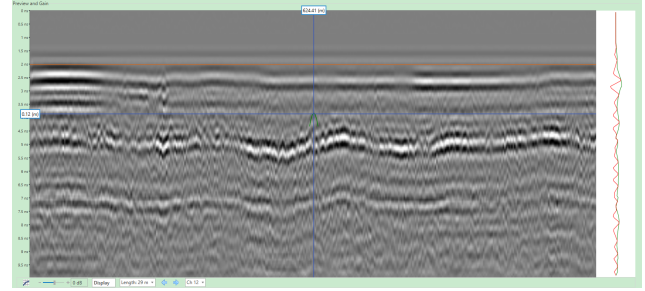
(a) 2 (dB)



(b) 10 (dB)



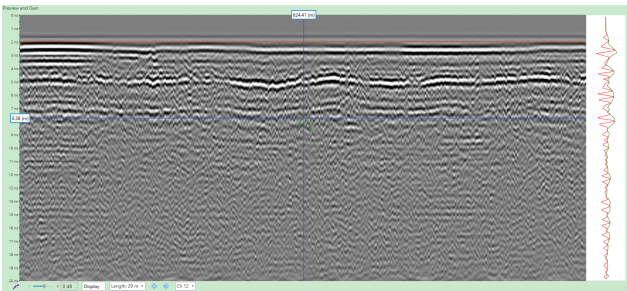
(c) 25 (dB)



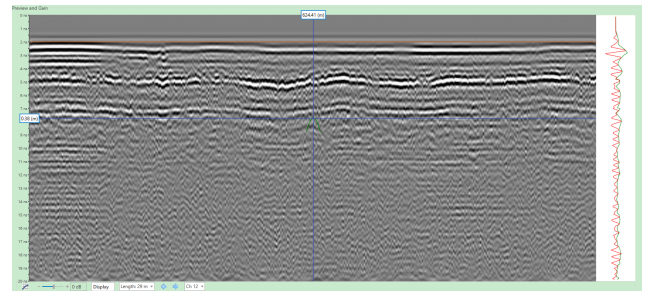
(d) 40 (dB)

Figure 2.4: Interference suppression with power limit value

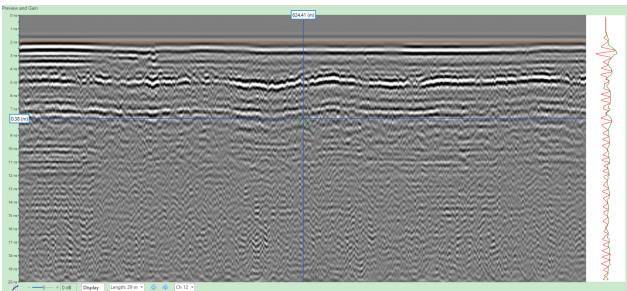
As is observed, the varying power limit value does not make too much difference for data in the very shallow subsurface. If a larger time window is selected, for example 20 (ns), the results are shown in Figure 2.5a - 2.5d.



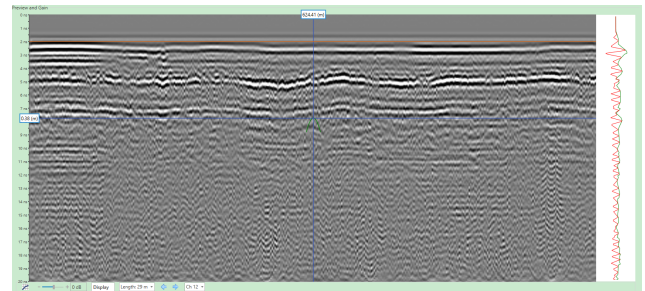
(a) 2 (dB)



(b) 10 (dB)



(c) 25 (dB)



(d) 40 (dB)

Figure 2.5: Interference suppression of the deeper subsurface with power limit value

Small differences can still be observed at the bottom-right corner, though they do not differ much from each other. The interference is still visible in the bottom-right corner of sub-figure (d) with the power limit of 40 (dB), while it is almost fully removed when the value is 10 (dB). This can be explained because the smaller the value is, the larger

the degree of interference removal will be. According to the guide<sup>4</sup>, however, too small values are also not recommended to use in order to avoid excessive removal, unless the data requires so. Thus, values around 10 (dB) or the default value 16 (dB) are good choice for the interference suppression filter.

#### 2.2.4 IFFT/ISDFT

Both the inverse fast Fourier transform (IFFT) and the inverse selective discrete Fourier transform (ISDFT) convert the data from the frequency domain to the time domain. Either of them can be used, and the main difference is that the constant bandwidth is used in the calculation of IFFT while in ISDFT the contribution of samples at high frequency gradually decreases as the time increases<sup>5</sup>. Thus, ISDFT could theoretically help obtain more reasonable data due to the increased signal-to-noise ratio at larger depths, though this is not of great significance in our case. Thus, all figures shown in this section were obtained with the application of ISDFT, as an exploration and comparison of filtering effects on Lekdijk data, while the A1 data were processed by applying the road template, containing the IFFT filter.

#### 2.2.5 Background removal filter

This filter removes the sort of background in the radar images, constituted by secondary reflections in the radar system<sup>6</sup>. Empirically, most parameters are kept as the default value while the only one to tune is the start time, named as 'Start Depth (ns)' in Examiner. In our case, the depth of the air-asphalt surface interface, indicated by the first strong reflection from the top, varies between 2-4 (ns). Thus, it is fine to set the start depth value also within this range, while the default value 4 (ns) is good. The suitable values for the transition zone are also within the same range, and the default value of 2 (ns) is fine. The filter length and the percentage of removal are both kept as default values. For the filter mode, the sliding window mean is the commonly used one while empirically the high-pass can also be helpful to look into the asphalt layers. A comparison is made between the two modes, with the rest parameters kept as the same, as shown in Figure 2.6a and 2.6b.

---

<sup>4</sup>The 'guide' from now on refers to the '3D-Radar Examiner 3 Data Processing Guide (Document version: 3.2.0)', which is attached in 'Local Resources' in Examiner.

<sup>5</sup>referring to the guide

<sup>6</sup>The 'background' here is explained in the guide as follows: 'Ground penetrating radars need to handle a very large dynamic range, as the power of a radar signal is reduced proportionally to the square of the target's distance from the antenna. Faint reverberations of high amplitude, early signals like the cross-talk transmitter-receiver or the surface reflection are usually quite visible compared to weak signals from deeper reflectors, and it is not possible to completely eliminate such secondary reflections in the radar system. These reflections constitute a sort of background in the radar images. Just like the originals, these echoes have little variability along the radar profiles and can be reduced through a background removal filter.'

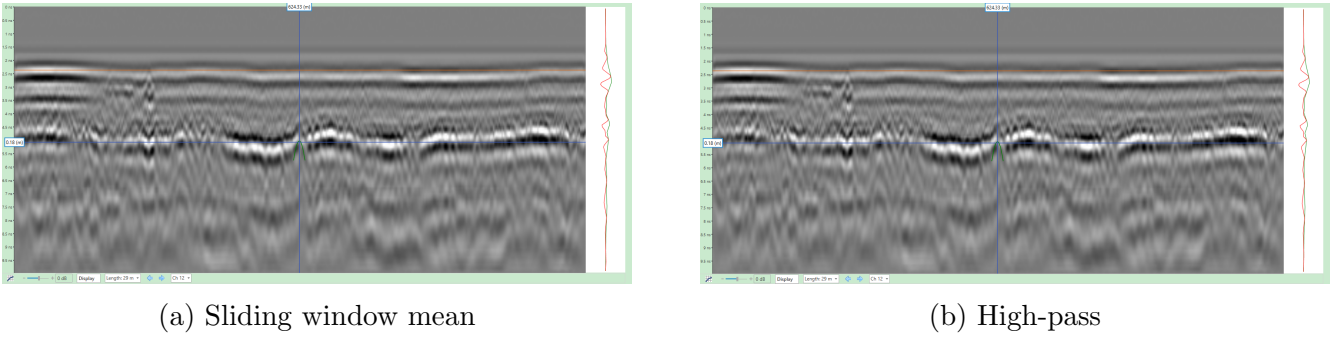


Figure 2.6: Background removal filter with the window type

As is observed, the results are similar with each other. Thus, it is fine to keep the default settings, but the high-pass filter can also be the alternative choice.

Moreover, the second background removal filter can be added to apply the filters in cascade to obtain radar image with higher quality, as is shown in the road template. As an example, a comparison was made between the images with and without the second filter (with the same default values as the corresponding one in the road template), as shown in Figure 2.7a and 2.7b.

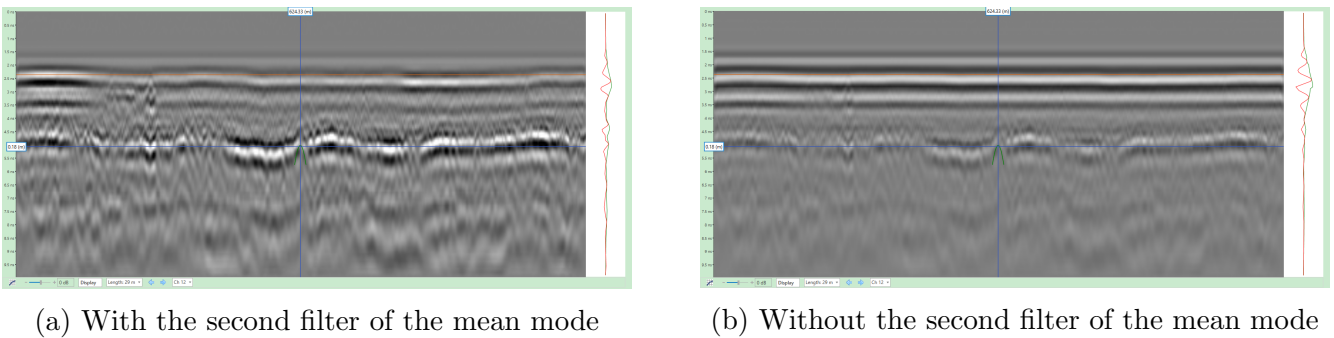


Figure 2.7: Background removal filter

It can be clearly viewed that the image with the second mean filter gives much better results than the one without it, as the horizontal lines are still quite visible in the upper part of the latter, due to minute differences in the background between the channels of the array<sup>7</sup>. Thus, the second filter is kept, as shown in road template, with the parameters as mentioned.

## 2.2.6 Summary of inbuilt filters

As is shown above, the tuning of the parameters in general aspects and the main filters does not make too much difference to the shallow subsurface of radar image in our case. Filters like gradual low pass filter and migration (Kirchhoff) are empirically not of great importance for shallow subsurface data, and thus are not applied in the default settings of the road template. In fact, in most cases for the shallow subsurface in asphalt engineering, the performance of default settings of the road template is

<sup>7</sup>referring to the guide

already fine.

However, the exploration of the inbuilt filters probably indicates their way of working that they filter the radar data based on certain way of numerical modification<sup>8</sup>.

For example, for the interference suppression, the parameter of power limit value, as discussed before, represents a certain threshold to control degree of suppression numerically.

Another example is the background removal filter, whose different window types probably mean different functions of removal and this explains why different effects of filtering are obtained given the same 'background' as discussed. For example, just as a deduction, when the mean filter mode is selected, it works in the way that a constant value, corresponding to the 'mean', is subtracted from every element of the matrix numerically representing the 'background' as discussed, and thus the 'background' is removed to a certain degree and the radar profile is thus filtered. When it comes to any other filter mode, a corresponding function is probably used for calculating the value to be subtracted from each matrix element before the subtraction is conducted. Then, I would like to make an attempt to create my own filters with a different way of working, which is further discussed in the following chapter.

---

<sup>8</sup>Of course the exact mechanisms of the inbuilt filters in Examiner are unknown for me as I don't have access to the source code of them, but the point could be indicated by some performances of filtering as mentioned.

# Chapter 3

## Filters

### 3.1 The way of filtering

The way of working of the inbuilt filters in Examiner is probably based on numerical modifications, as discussed in the previous section. However, I want to make an attempt to realize radar image data filtering in a different way of working, i.e. to filter the image data principally instead of purely numerically.

Take the deconvolution (decon) filter as an example. First of all, it is based on the assumption that the GPR signal represents the convolution of a reflectivity series with a stationary wavelet plus some noise:

$$x(t) = r(t) * w(t) + n(t) \quad (3.1)$$

where  $x(t)$  is the measured GPR signal,  $r(t)$  is the reflectivity series while  $n(t)$  is the noise. Under the other assumption that  $n(t)$  is negligible since it is uncorrelated with  $r(t)$  and its variance is comparatively quite small, the relation holds:

$$x(t) = r(t) * w(t) \quad (3.2)$$

and then when the inverse filter  $f(t)$  satisfying

$$\delta(t) = f(t) * w(t) \quad (3.3)$$

is computed, it can be applied to both sides of eq.(3.1) to obtain further results [16][18].

Thus, the GPR data is efficiently filtered with the application of the decon filter, principally removing the influence of reflections, once the assumptions are satisfied to a large degree.

Of course numerical techniques are always required in any filter, but the point is that I would like to find a model, theory, etc., which the principle of my data filter is based on, instead of purely depending on numerical modifications with no science behind it.

## 3.2 The model system

In the research work of Lambot et al.[7], a model has been raised. The subsurface is viewed as a multilayered medium as shown in Figure 3.1:

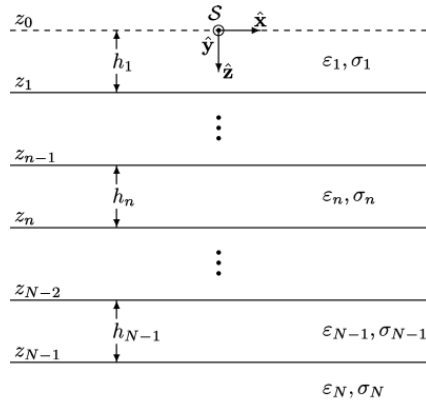


Figure 3.1: Multilayered medium with point source

while the antennas are viewed as a point, which is further discussed in section(3.4). The model system is shown in Figure 3.2:

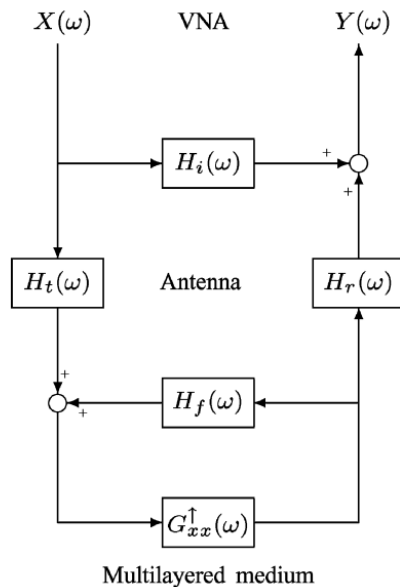


Figure 3.2: The linear system model in series and parallel of the VNA-antenna-multilayered multilayered system

describing the relationship between the reference plane, the antennas and the subsurface, which has added a positive feedback block  $H_f(\omega)$  to previous work of Lambot et al. [5][6], and the corresponding frequency domain relationship between the measured radar data and the impulse response, i.e. the uncontaminated radar data, is expressed as follows:

$$S_{11}(\omega) = H_i(\omega) + \frac{H(\omega)G_{xx}^\uparrow(\omega)}{1 - H_f(\omega)G_{xx}^\uparrow(\omega)} \quad (3.4)$$

where  $\omega$  is the frequency,  $S_{11}(\omega)$  is the measured data, and  $G_{xx}^\uparrow(\omega)$  is the Green's function, which is principally a specific solution to the Maxwell's equations, indicating the impulse response, while  $H_i(\omega)$ ,  $H(\omega)$  and  $H_f(\omega)$  are three transfer functions.  $H_i(\omega)$  is the return loss transfer function representing the part of ringing corresponding to the multiple wave reflections occurring within the antenna, indicating the interaction between the antenna and the air, and  $H(\omega)$ , which is defined as  $H(\omega) = H_t(\omega)H_r(\omega)$ , means the multiplication of the transmitting and receiving transfer functions  $H_t(\omega)$  and  $H_r(\omega)$  representing the antenna gain and phase delay between the measurement point and the source and receiver virtual point, which can be understood as the influence on measurement due to the radar antennas themselves. The transfer function  $H_f(\omega)$  describes the part of the backscattered field that is reflected back again towards the surface, indicating the multiple wave reflections between the antennas and the subsurface [7].

The radar system used in our case is also a combination of a monostatic ultrawideband (UWB) stepped-frequency continuous-wave (SFCW) radar with a monostatic air-coupled antenna, with the same conditions as the one used in the previous research work as mentioned. Moreover, the subsurface to measurement is asphalt layers of road sections in our case, which could more or less be viewed as the multilayered medium. Thus, I referred to this model as the theoretical basis, based on which I would like to make an attempt to obtain the radar data filters principally. The three transfer functions as mentioned are the filters I aim to obtain, which is further discussed in the following section.

### 3.3 Filters and the Green's function

#### 3.3.1 Impulse response calculation

Once the three transfer functions  $H_i(\omega)$ ,  $H(\omega)$  and  $H_f(\omega)$  are known, the impulse response  $G_{xx}^\uparrow(\omega)$  of the measured radar data  $S_{11}(\omega)$  in the frequency domain can be solved straightforwardly, according to the aforementioned formula, as:

$$G_{xx}^\uparrow(\omega) = \frac{S_{11}(\omega) - H_i(\omega)}{H(\omega) + (S_{11}(\omega) - H_i(\omega))H_f(\omega)} \quad (3.5)$$

Thus, to filter the measurement data, I have to obtain the three transfer functions first, which will be mentioned as three filters from now on.

#### 3.3.2 The matrix system

The aforementioned relationship can be written as the form:

$$H_i(\omega) + G_{xx}^\uparrow(\omega)S_{11}(\omega)H_f(\omega) + G_{xx}^\uparrow(\omega)H(\omega) - G_{xx}^\uparrow(\omega)H_i(\omega)H_f(\omega) = S_{11}(\omega) \quad (3.6)$$

which can be written in a matrix-vector-vector system form as follows when one more parameter, the height  $z$ , is taken into account during the measurement:

$$\begin{pmatrix} 1 & G_{xx}^\uparrow(\omega, z_1)S_{11}(\omega, z_1) & G_{xx}^\uparrow(\omega, z_1) & -G_{xx}^\uparrow(\omega, z_1) \\ 1 & G_{xx}^\uparrow(\omega, z_2)S_{11}(\omega, z_2) & G_{xx}^\uparrow(\omega, z_2) & -G_{xx}^\uparrow(\omega, z_2) \\ \dots & \dots & \dots & \dots \end{pmatrix} \times \begin{pmatrix} H_i(\omega) \\ H_f(\omega) \\ H(\omega) \\ H_i(\omega)H_f(\omega) \end{pmatrix} = \begin{pmatrix} S_{11}(\omega, z_1) \\ S_{11}(\omega, z_2) \\ \dots \end{pmatrix} \quad (3.7)$$

where  $z_1, z_2$ , etc. represent different heights. Then the three filters can be obtained by solving this matrix-vector-vector system, given the measured data and the Green's function.

Thus, the number of heights determines the number of rows in the matrix while the number of matrix systems to solve corresponds to the number of frequencies.

### 3.3.3 The Green's function for specific cases

Two specific cases have been considered, regarding the solution:

The first one is the sky-shot measurement, where the radar system shots towards the sky, i.e. a free space with no obstacles to the propagation of electromagnetic (EM) waves. In this case the Green's function  $G_{xx}^\uparrow(\omega, z) = 0$ , and the measurement data  $S_{11}(\omega, z)$  is therefore just the sky-shot data  $H_i(\omega, z)$ .

The measurement on a metal plate is the second specific case, where the Green's function is known as the following analytical form<sup>1</sup>:

$$G_{xx}^\uparrow(\omega, R) = \left( \left( \frac{\omega}{c_0} \right)^2 - \left( \frac{1}{R^2} + i \frac{\omega}{c_0 R} \right) \right) \frac{\exp(-i \frac{\omega R}{c_0})}{4\pi i \omega \epsilon_0 R} \quad (3.8)$$

where  $R$  is the path length of the EM wave from the source point to the receiver point, which is:

$$R = \sqrt{\Delta x^2 + 4h^2} \quad (3.9)$$

where  $\Delta x$  is the offset between the source and the receiver antenna and  $h$  is the height of the measurement point to the metal plate assuming the source and the receiver point has the same height, and  $\omega$  is the angular frequency of the signal, and  $c_0$  and  $\epsilon_0$  are respectively the propagation velocity of light in air and the absolute dielectric constant of air, while  $i$  is the imaginary unit.

All quantities in the matrix on the left hand side (LHS) and the vector on the right hand side (RHS) are known, and the solution can be obtained. Although principally only 3 heights are required to get a solution, data at more heights should be used to

<sup>1</sup>The expression for this specific case is not something that can be easily found in papers or textbooks. The deduction of it is written in Appendix A.

obtain the solution with more robustness while the rest data at more heights could be used for checking the solution, which will be further discussed later.

For the two measurements, three measurement settings as mentioned before, were applied, corresponding to the Setting A in A1 of day 1 (105 (cm) distance, 25 (ns) time window and 1.0 ( $\mu\text{s}$ ) dwell time), Setting B in A1 of day 2 and day 3 (101 (cm) distance, 25 (ns) time window and 1.0 ( $\mu\text{s}$ ) dwell time)<sup>2</sup> and the Setting C (Setting 1, as mentioned before) respectively. Since setting C is the same as the normal setting at the Lekdijk, the data obtained with this measurement setting were exported for processing in this part.

### 3.4 Assumptions

To obtain my own filters based on the model and the data from the two specific measurements as mentioned, some assumptions should be satisfied to a great degree: The first assumption is that the ground surface is in the far field of the antennas, and the source and the receiver antennas can be modeled as a point.

The metal plate, correspondingly, can be viewed as an infinitely extensive 2D platform. Moreover, since the source radiation pattern is not needed for the antenna modeling under a monostatic configuration as the picked up signal only propagates along the direction of the antenna axis, the antenna can thus be modeled as a linear system [6]. The source and the receiver antennas are also assumed at the same height and also have no offsets along the dimension of their own extension, i.e. y-direction, and the offset only exists in the x-direction. The antenna heights and directions are shown later in Figure 3.5.

## 3.5 The sky-shot and the metal plate measurements

### 3.5.1 Sky-shot measurement

In this measurement, the 3D - radar was turned up-side-down, with the antennas pointing to the sky, as is shown in Figure 3.3:

---

<sup>2</sup>These two settings used in A1 have a higher measurement speed than those used in Lekdijk.



Figure 3.3: The sky-shot measurement

measuring the response of the air to the EM waves.

There was no need to change the antenna heights in this measurement, and since it was inconvenient to move the system in this case, we used a cable connecting the DMI and the antennas and circulated the DMI artificially to simulate the moving of vehicle, generate the distance and acquire the measurement data.

### 3.5.2 Metal plate measurement

In the second measurement, the radar was placed above a metal plate to obtain the data of the strongest reflection that could be obtained, which was coupled to the front of the vehicle, as shown in Figure 3.4a and 3.4b.



(a) The side view



(b) The straight view

Figure 3.4: The metal plate measurement

The in-line measurement distance of the metal plate was ca. 5.35 m while the width was ca. 1.64 m. The height of the bottom of the radar to the ground varied between

15 cm and 25 cm, with the step size 1 cm, as shown in Figure 3.5<sup>3</sup>.

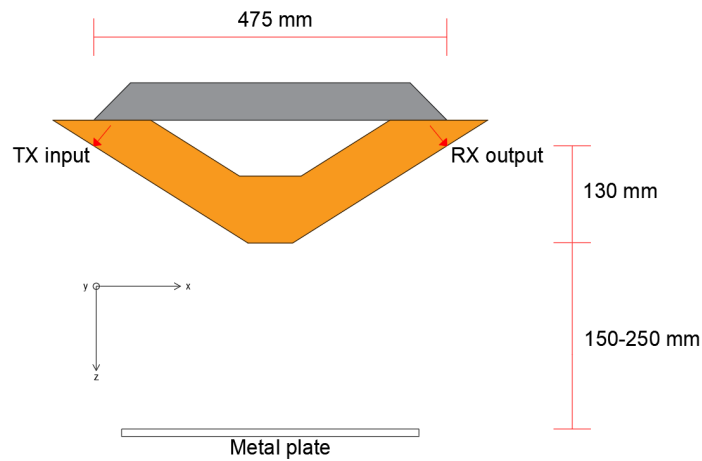


Figure 3.5: Antenna dimensions and directions

x-direction is the direction of the in-line measurement, and the antennas extend in the y-direction while z-direction points vertically downwards into the subsurface.

Regarding the way of distance covering in this measurement, driving the vehicle over the metal plate was chosen, instead of turning the DMI artificially as mentioned before, to better simulate the real measurement on road sections. Three measurements, corresponding to the three settings respectively, were conducted at each height as mentioned.

### 3.6 Measurement data processing

After data acquisition, both the sky-shot and the metal plate data were exported from the Examiner and imported to MATLAB (R2022a - academic use). They were read as matrices and were transposed afterwards so that the number of rows of the matrices represents the number of time samples (t in (ns)) while the number of columns corresponds to the in-line measurement distance samples (x in (m)).

It was found that the metal plate data at 15 (cm) height slightly differed in the number of traces in x - dimension. Thus this data was discarded for the consistence of matrix size, and the metal plate data at 10 heights from 16 - 25 cm, 1 cm interval, were stored.

#### 3.6.1 Channel average and trace average

After the importing, both measurement data were channel averaged and then trace averaged.

The former is due to the fact that the measurement data obtained at different channels probably differ from each other even if the conditions of the measurement environment were the same everywhere because the antennas at distinct channels might be slightly

<sup>3</sup>This figure was made by ing. R.H. van Beuningen.

different from each other, not to mention varying conditions in real measurement environment.

For example, the sky-shot measurement was conducted in a comparatively open space, but not exactly no variations in it while for the metal plate measurement the situation was even worse since the antennas located at the channels close to the sides of the radar did not satisfy the aforementioned assumptions of the model as well as the ones around the center of the radar. Thus, for both measurements, I only took the data from the 3 channels in the middle of the 25 channels to calculate the channel averaged profile.

The latter is because the measurement data were not constant on all traces along the distance dimension, which is further shown in Figure 3.6, and thus only the traces in the middle of the distance dimension, with comparatively constant data, were taken and then trace averaged. I took the middle 12 traces out of the total 72 traces for all measurement data.

### 3.6.2 Time domain data at different heights

After the channel and the trace average, the profiles of the sky-shot measurement and the metal plate measurement at 16 (cm) height is shown visualized as examples, as shown in Figure 3.6a and 3.6b.

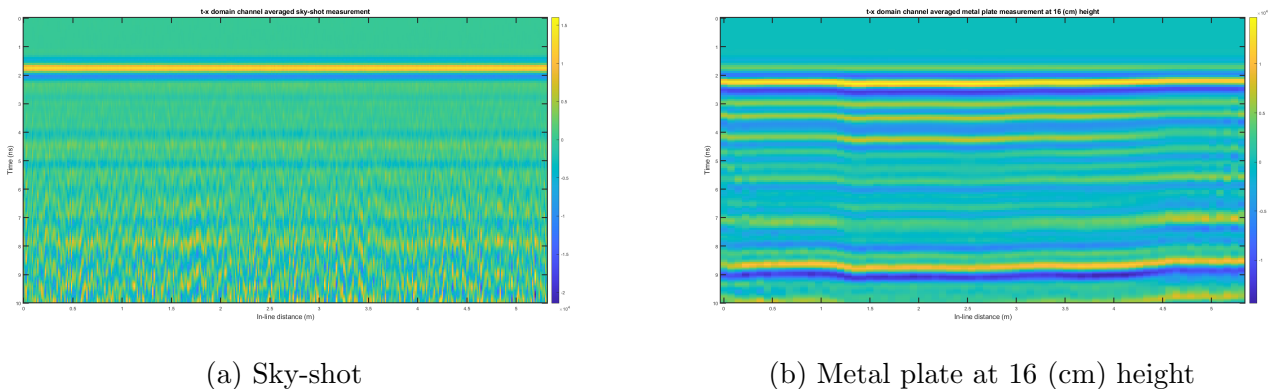


Figure 3.6: Examples of t-x domain measurement data profile

As is observed in the sky-shot profile, the patterns at different traces are not exactly constant but slightly varying while this is also observed in the metal plate profile, and the multiples are not completely horizontally straight and parallel to each other. These phenomena indicate some probable inaccuracies in measurements.

The metal plate data in the time domain (t-x) at different antenna heights are also visualized, as shown in Figure 3.7.

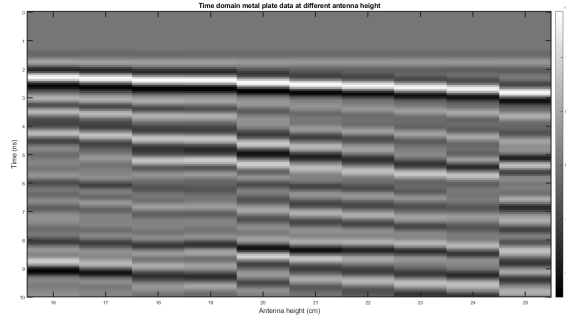


Figure 3.7: Time domain metal plate data at various heights

The straight line first appearing in time indicates the direct wave, followed by the first strong reflections as shown by the strongest patterns in the image, while the later ones are the multiples.

The general aspects of the image pattern seem to be normal, compared with the counterpart in the work of Lambot et al. [7] as a reference, as shown in Figure 3.8 as follows.

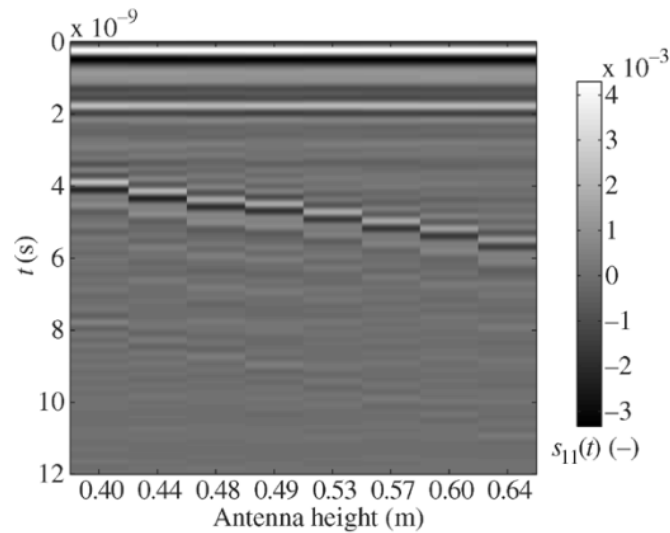


Figure 3.8: Time domain metal plate data at various heights by Lambot et al.

However, some details of the pattern indicate that the measurement was still not accurate enough somewhere. For example, the data corresponding to antenna height of 18 (cm) and 19 (cm) do not differ much from each other, indicating that these two heights were probably not measured accurately enough.

As a check for the aforementioned analytical expression of the Green's function in this case, the values at various frequencies and heights were calculated. Then I applied an IFFT to it, and the time domain data with various heights are shown in Figure 3.9a and 3.9b.

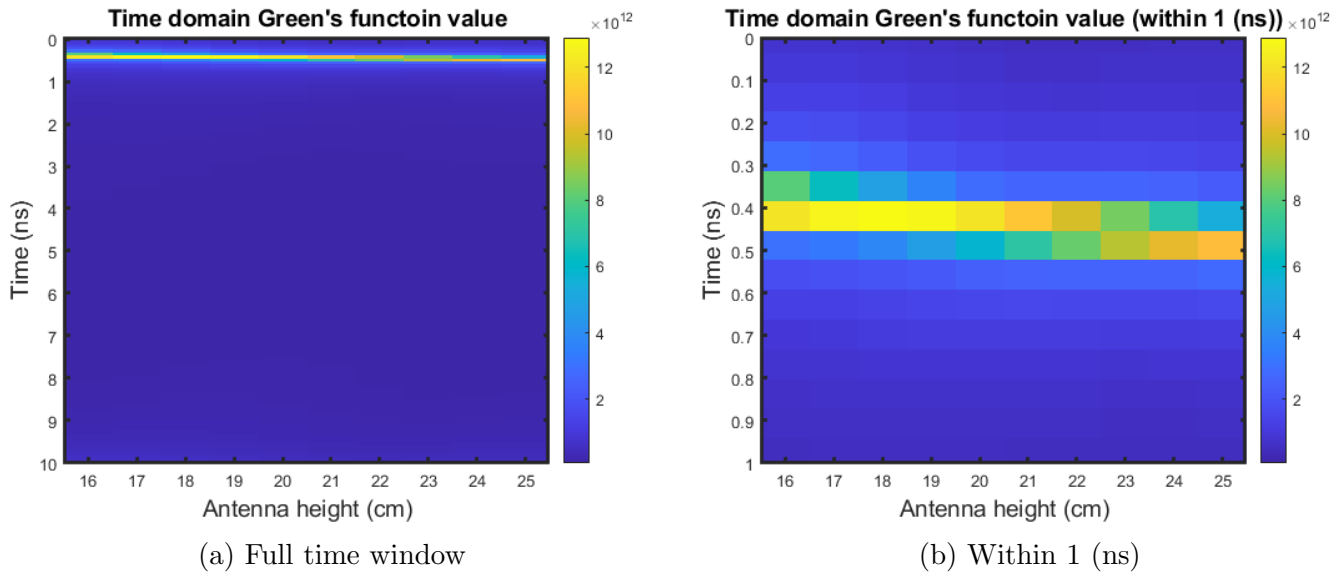


Figure 3.9: Time domain Green's function value at various heights

By comparison, the result in the work of Lambot et al.[7] is shown in Figure 3.10 as follows<sup>4</sup>.

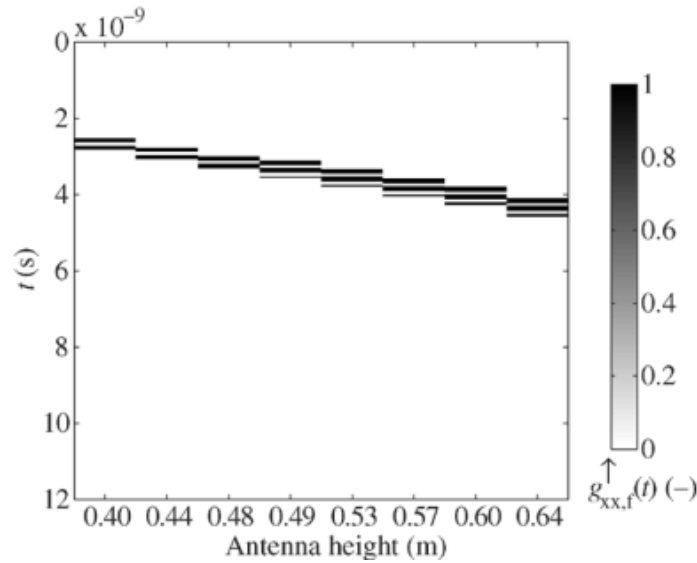


Figure 3.10: Time domain Green's function value at various heights by Lambot et al.

### 3.6.3 Frequency domain spectrum

The Fast Fourier Transform (FFT) is conducted to the channel averaged sky-shot data and the metal plate data at a certain height in the t-x domain to the t dimension, and the corresponding spectrum in the frequency domain (f-x) is obtained, as shown in Figure 3.11a and 3.11b.

<sup>4</sup>Notice that the result by Lambot et al. is the filtered signal using the antenna model, and the amplitude is also normalized, instead of the result of direct calculation with the expression in our case. The figure is placed here just for the comparison of pattern.

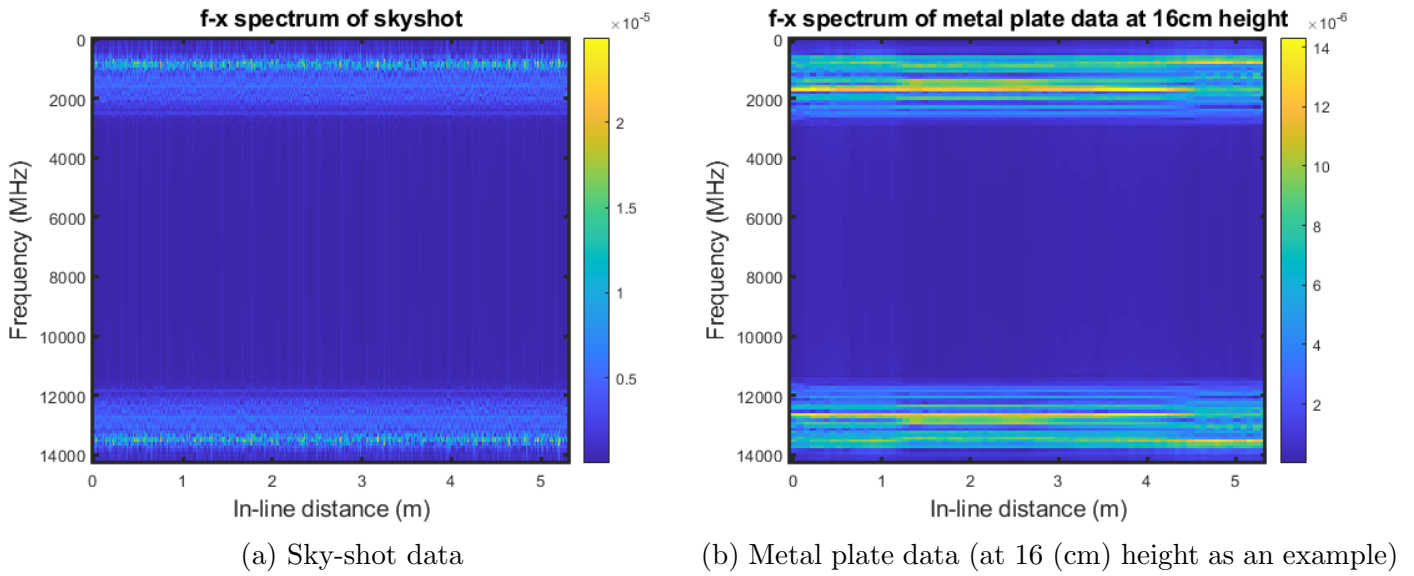


Figure 3.11: f-x domain spectrum of the two measurement data

As is observed, the channel averaged profiles of both measurement are not exactly constant at all traces along the distance dimension, especially the metal plate data, and this is why only the traces in the middle were chosen for calculating the following trace average. The Nyquist criterion  $f_s > 2f_{max}$ , with the  $f_s$  and  $f_{max}$  representing sampling frequency and maximum frequency, is satisfied.

The aforementioned measured radar data  $S_{11}$  is just the trace averaged metal plate data in our case, as a function of time and antenna height, which is plotted in Figure 3.12.

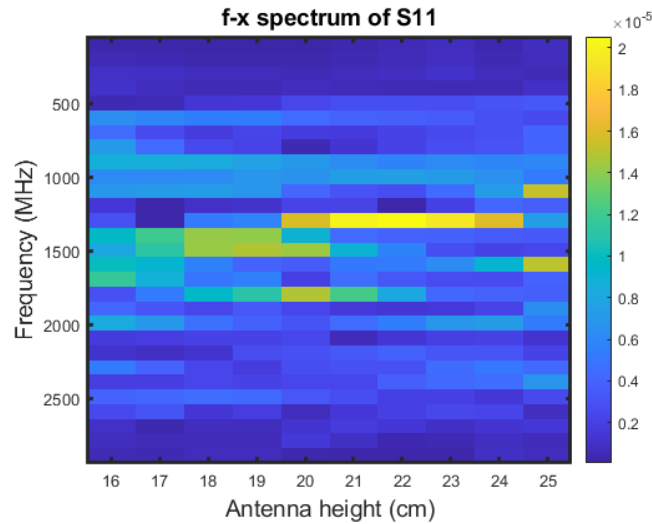


Figure 3.12: f-x domain spectrum of  $S_{11}$

The channel averaged sky-shot data were also followed by a trace average, which became a vector as a function of frequency.

## 3.7 Checking the solution

After the filters were obtained by solving the matrix systems as mentioned before, they should be checked before being applied to filter other data.

### 3.7.1 Robustness check

During the metal plate measurement, at least 3 among all 10 heights, the 15 (cm) height data discarded, are required to solve the matrix equation in order to obtain the solution since there are three unknown filters to be solved, although more are needed to ensure the robustness of the solution.

I solved the matrix systems by using data from all heights (16:1:25 (cm)), the first 5 heights (16:1:20 (cm)), the last 5 heights (21:1:25 (cm)) and the 5 intermediate heights (16:2:24 (cm)) respectively, and made a comparison between the sky-shot filters, i.e. the first element of the solution vector, obtained by different solutions. Since there are complex numbers in the frequency domain, the magnitude of the sky-shot filters were compared, as shown in Figure 3.13. For completeness, the measured sky-shot data were also plotted in dashed line.

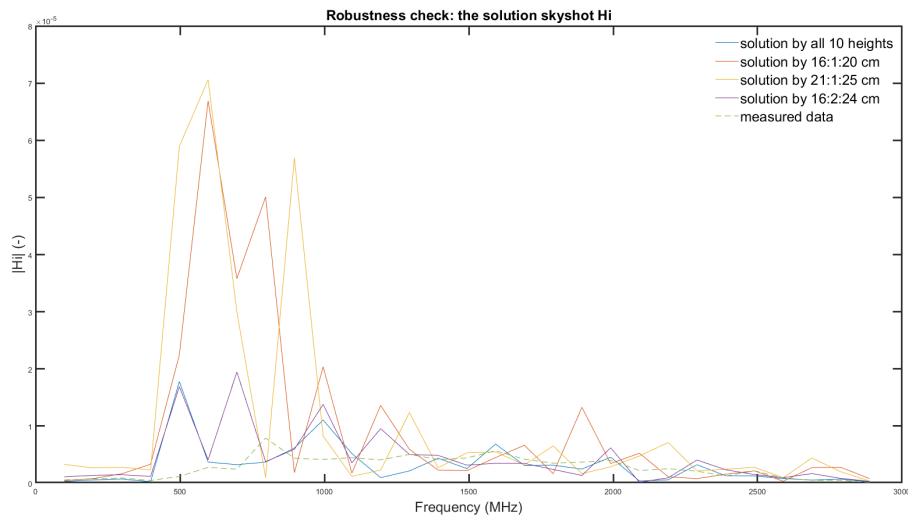


Figure 3.13: The robustness check

As is observed, the different solutions already differ from each other clearly in magnitude, indicating that the robustness of the solution is not satisfactory.

### 3.7.2 Bias check

I also checked the relative error of the magnitude of  $H_i$  solved by data from different heights, as mentioned above, to that of the measured  $H_i$ , indicating the degree of the bias of the solution to the measured value. The results are shown in Figure 3.14.

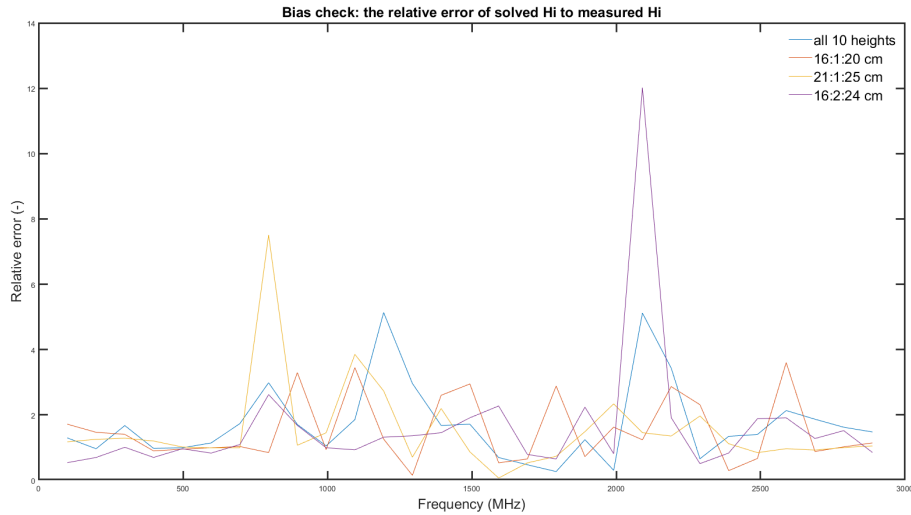


Figure 3.14: The bias check

Large relative errors are observed, indicating that the degree of bias of the solution to the measured data is also large.

### 3.7.3 Pattern check

To check the general patterns of magnitude of the solved filters as a function of frequency, the three transfer functions which were solved are plotted in Figure 3.15a, 3.15b and 3.15c respectively as follows.

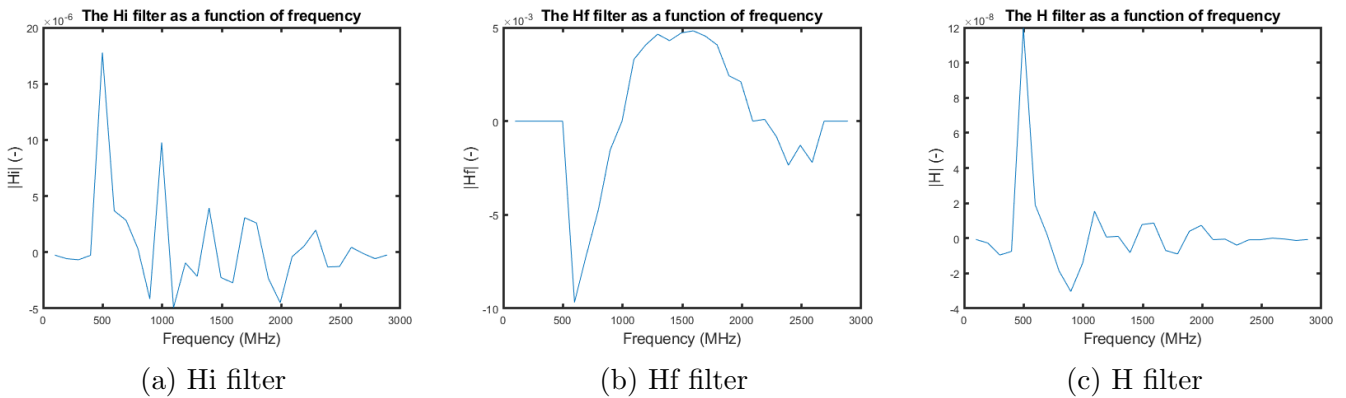


Figure 3.15: Pattern check

By comparison, the counterparts in the work of Lambot et al. are shown in Figure 3.16a, 3.16b and 3.16c.

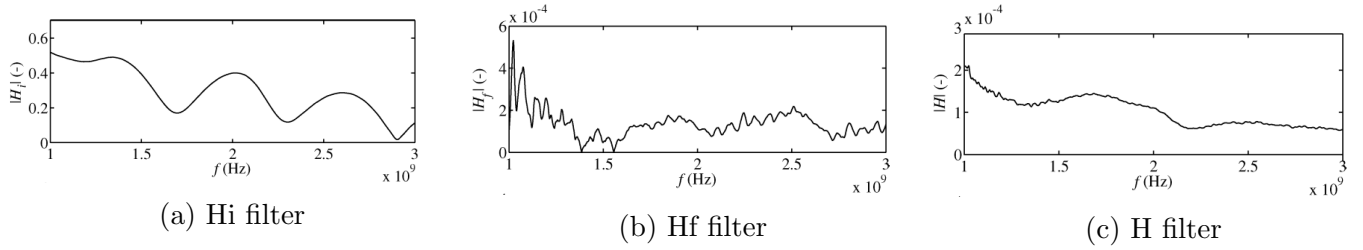


Figure 3.16: Pattern check: patterns of the filters in previous work

As is observed, clear differences can be observed between the magnitude patterns of the filters I have solved and those obtained in previous work.

### 3.8 Discussion and analysis on the results

As is observed from the aforementioned results, the solved filters generally do not show a great performance in either robustness or unbiasedness, and their magnitude patterns also differ from what was obtained in previous work.

Thus, they are not adequate to be applied to other measurement data for data filtering at the moment, but the reasons behind this are worth considering.

Of course there existed some errors during our measurement, but what is probably most responsible for such results are the ones that broke the assumptions of the model. For example, the metal plate is too small in area, which didn't fulfil the infinite extent assumption, or the radar system is by comparison too large to be simplified as a point source, considering our measurement height, and the metal plate is thus not completely in the far field either.

The other important reason might be the data exported from the Examiner. There are only 29 frequency samples within the bandwidth of our measurement in each of the exported matrix. The large interval on frequency axis, i.e. the low sampling rate, has probably also contributed to the biased results.

What this attempt has provided is an application of the method to obtain the filters based on the model as well as the points worth noticing and avoiding when making this application, which is further discussed in the last chapter.

# Chapter 4

## Application of machine learning methods

If the delaminations in asphalt layers can be detected automatically by algorithm, then the workload of asphalt engineers will be alleviated. Plenty of research work has been conducted regarding the asphalt damage problems on the surface of road sections with machine learning methods, for example, the stripping of asphalt coating [17], the automatic detection of damage on the surface of the asphalt<sup>1</sup> [12], etc.. But when it comes to the detection of damages within asphalt, comparatively much smaller amount of research work has been conducted.

I applied machine learning methods to images selected from the A1 data to explore their performance on our radar images in terms of indication, recognition as well as detection of damages within asphalt.

### 4.1 Expectation maximization

Firstly, based on the idea that if the interesting parts in a radar profile can be, to some extent, highlighted or separated, then the asphalt engineers can know at least which part to put more focus on, I made an attempt to conduct the image segmentation with the expectation maximization (EM) algorithm.

#### 4.1.1 Principle

The core of the EM algorithm is an iterative method of finding maximum likelihood estimate of certain parameters. For an image segmentation problem, these parameters are the ones for the Gaussian clustering to which the points in the feature space belong, including the means vector, the covariance matrices and the weights corresponding to different Gaussian distributions.

The iteration includes the E - step (expectation) and the M - step (maximization). In the E - Step, the values of these parameters are first initialized and then estimated (conditional expectation), based on which the maximum likelihood data is estimated in the M - step. The iteration stops until certain condition is met, for example, either

---

<sup>1</sup>The damages on the surface of asphalt road sections. For example, just like the ones shown in our visual inspection in Figure 1.4.

the differences between the values obtained by these two steps being small enough, i.e. convergence, or the number of iteration reaching the maximum number as set [1].

Besides the intuition of alternating between variables, the EM algorithm can also be explained as well as derived in different ways, and one of them is lower bound maximization [10][11]. From this point of view, a derivation, together with the explanation, was given by Dellaert [3], closely following the work of Minka [10], with the key points as follows:

To maximize the posterior probability of the parameters  $\Theta$ , based on the given data  $U$ , in the presence of hidden data  $J$ , is equivalent to maximize the logarithm of the joint distribution  $P$  as it is proportional to the posterior:

$$\Theta^* = \operatorname{argmax} \log P(U, \Theta) = \operatorname{argmax} \log \sum_{J \in J^n} P(U, J, \Theta) \quad (4.1)$$

The lower bound is constructed as:

$$B(\Theta; \Theta^t) = \sum_{J \in J^n} f^t(J) \log \frac{P(U, J, \Theta)}{f^t(J)} \quad (4.2)$$

The distribution  $f^t(J)$  is solved by calculating the derivative of an objective function as:

$$f^t(J) = \frac{P(U, J, \Theta^t)}{\sum_{J \in J^n} P(U, J, \Theta^t)} = P(J|U, \Theta_t) \quad (4.3)$$

The E-step calculates:

$$f^t(J) = P(J|U, \Theta_t) \quad (4.4)$$

while the M-step maximizes the bound:

$$\Theta^{t+1} = \operatorname{argmax}[Q^t(\Theta) + \log P(\Theta)] \quad (4.5)$$

It can be proved that the EM algorithm converges to a local maximum of  $P(U, \Theta)$ , and equivalently maximizes the log-posterior  $\log P(\Theta|U)$  [3][9].

### 4.1.2 Selection of training data and parameter

The number of mixture components  $K$ , ideally, could be chosen as the value that best suits the natural number of groups present in the image [2]. In our case, it's selected as 3 by trial. Since the algorithm is mainly based on pixel color recognition, I started from the magnitude figure with the jet color mode, which is assumed to have generally one of the strongest contrasts between the pixels among all figure types (Real, Magnitude, Imaginary, Hybrid and Wiggle) and all color modes (Gray, Copper and Jet) in Examiner. The original figure is shown in Figure 4.1.

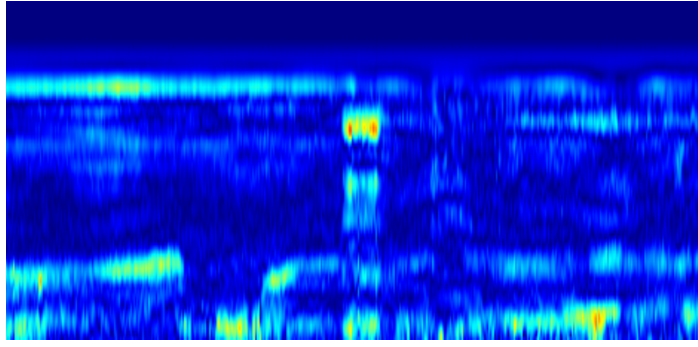


Figure 4.1: The training figure (A1L267, magnitude, jet)

This is the radar profile of the delamination A1L267. The structure in the middle is a delamination, verified by the borehole core sampling. Some regions are extracted from it as sources of training data for the machine to estimate the Gaussian parameters for features of the delaminations as well as other remarkable structures within asphalt that we are interested in, and non-features, i.e. the rest part that are not important for us.

Each pixel of these parts is converted and normalized to a row vector with three elements, representing the value in the channel of red (R), green (G) and blue (B) color respectively. For images with '.png' format there is also one optional alpha channel representing the degree of transparency, which was removed in our case. The training data for features and non-features were thus created, stored in a '.dat' file for my Python code to read later.

The training image, from which the training data is extracted from, just sa a trial, was first used for testing the performance of the algorithm.

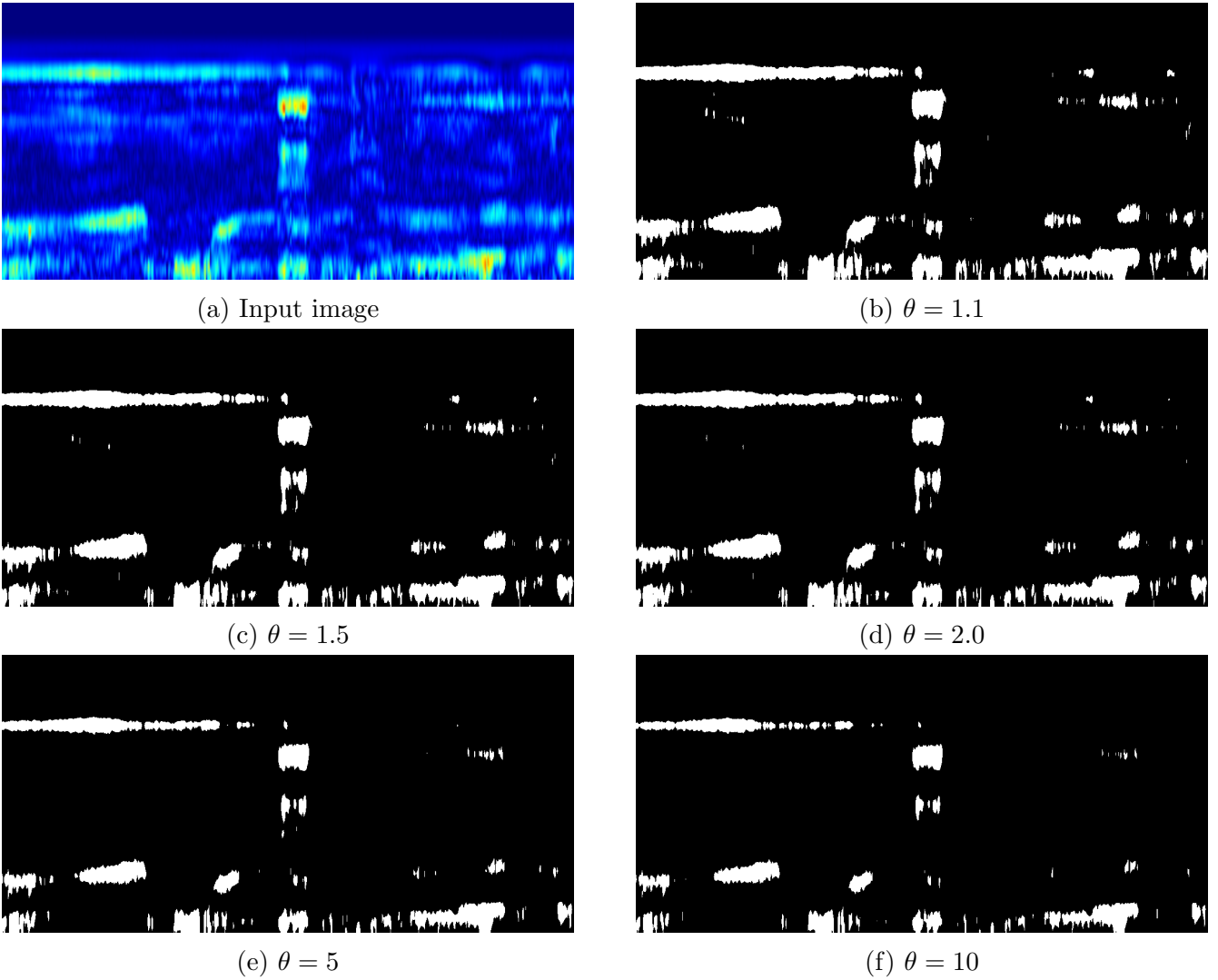


Figure 4.2: The result of feature detection

As shown in Figure 4.2a - 4.2f, the parameter  $\theta$  controls the threshold of segmentation - the larger the value is, the more strict the judgement of segmentation will be. As is indicated, most of the critical features as mentioned were highlighted with the white color, and then could be easily recognized by human vision. In addition, the choice of segmentation threshold value did not have much influence on the recognition of main structures in this case.

However, radar profiles with the aforementioned mode are not the ones that asphalt engineers most often work on. Thus, the real profile with gray color mode was then selected for training and recognition. The method of training data extraction was similar, but one point was that for images with gray color mode, it turned out that the three elements of the row vectors in the training data had exactly the same value, which would cause the numerical problem that the determinant of the covariance matrices would become zero. The solution was adding a random value on each value to avoid this problem. The results of detection, in comparison with the raw data, are shown in Figure 4.3a - 4.3f, corresponding to different values of the threshold parameter.

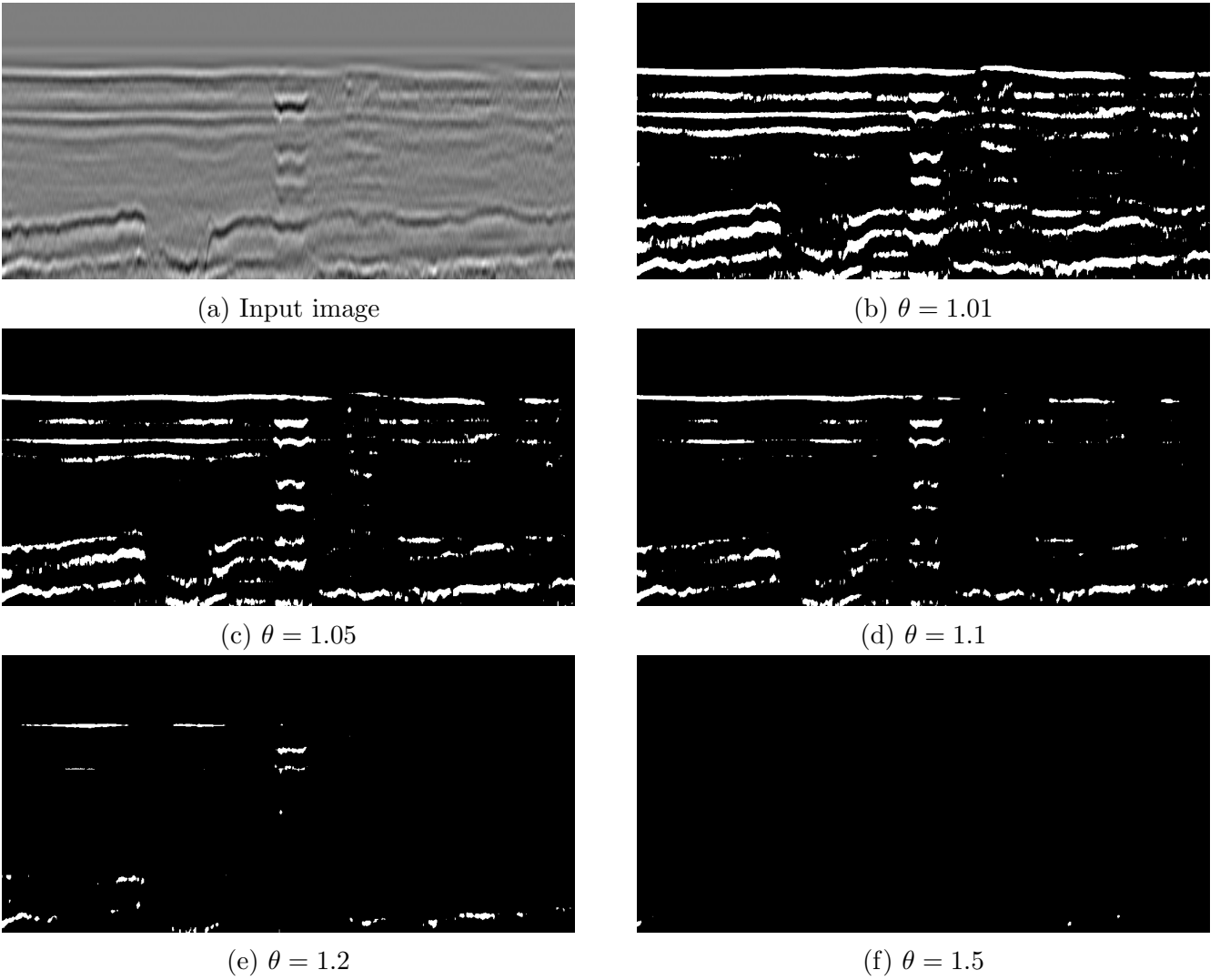


Figure 4.3: The result of feature detection (real)

As is indicated, when the input data became the real profile with the gray color mode, the results became sensitive to the selection of the value of  $\theta$ . When  $\theta = 1.01$  or  $1.05$ , most interesting features were highlighted, though more structures that were not that interesting were also included, while more of them were not recognized with the increasing value, as is especially shown in the sub-figures e and f.

Thus, it is shown that most of the interesting features, including the delaminations in the shallow subsurface, can be kind of 'roughly' recognized, in terms of highlighting, based on the EM algorithm with the suitable choice of the threshold parameter. However, the effect of segmentation still needs to be further tested by more images from our data. Moreover, one problem of this algorithm is also obvious: as this algorithm is based on pixel color segmentation, it detects all the features based on judgement relevant to the threshold and can hardly specifically recognize the delaminations only. In other words, the exclusive and automatic detection of delaminations, also the same for other kinds damages within asphalt, has not been completely realized by this algorithm yet. Because of the way the EM algorithm works, this problem cannot be decently overcome, and that is the reason why other kinds of algorithms are required

for this objective, which is further discussed in the following section.

## 4.2 Classification and object detection

The EM algorithm, as is shown above, has realized image segmentation, and thus the interesting parts of images are highlighted, reducing the workload of asphalt engineers trying to humanly recognize delaminations. However, it is not able to specifically recognize the delaminations structures exclusively. More accurately speaking, EM can only segment the whole image and highlighting the part that certain targets belong to while it can never accurately detect the targets. Thus, the object detection algorithm, is needed to further realize this goal.

### 4.2.1 Principles

DarkNet-53 is a convolutional neural network (CNN) module with originally 53 layers trained on ImageNet database<sup>2</sup>, whose architecture is shown in Figure 4.4 [13] as follows:

# Repeation	Type	# of filters	Size/Stride	Output Size
1	Convolution	32	$3 \times 3/1$	$256 \times 256$
1	Convolution	64	$3 \times 3/2$	$128 \times 128$
1	Convolution	32	$1 \times 1/1$	
	Convolution	64	$3 \times 3/1$	
	Residual			$128 \times 128$
1	Convolution	128	$3 \times 3/2$	$64 \times 64$
2	Convolution	64	$1 \times 1/1$	
	Convolution	128	$3 \times 3/1$	
	Residual			$64 \times 64$
1	Convolution	256	$3 \times 3/2$	$32 \times 32$
8	Convolution	128	$1 \times 1/1$	
	Convolution	256	$3 \times 3/1$	
	Residual			$32 \times 32$
1	Convolution	512	$3 \times 3/2$	$16 \times 16$
8	Convolution	256	$1 \times 1/1$	
	Convolution	512	$3 \times 3/1$	
	Residual			$16 \times 16$
1	Convolution	1024	$3 \times 3/2$	$8 \times 8$
4	Convolution	512	$1 \times 1/1$	
	Convolution	1024	$3 \times 3/1$	
	Residual			$8 \times 8$
	Avg_Pool			$1 \times 1$
	Connected		1000	
	Softmax			

Figure 4.4: Darknet-53 architecture

Five repetitive blocks are involved, each with two convolution layers of size  $1 \times 1$  and  $3 \times 3$ , followed by one Residual layer [13]. The purpose of Darknet-53 is the characteristics extraction of input images [8][13][14].

My work in this part is an application of the object detection algorithm YOLO v3 [15], which is based on a variant of Darknet-53 and has a 106-layer-fully-convolutional

<sup>2</sup>ImageNet. <http://www.image-net.org>. It includes images of a wide range of commonly observed categories, designed for visual object recognition research.

underlying architecture with 53 more layers are stacked onto the original layers for the task of detection, as is shown in Figure 4.5<sup>3</sup> as follows:

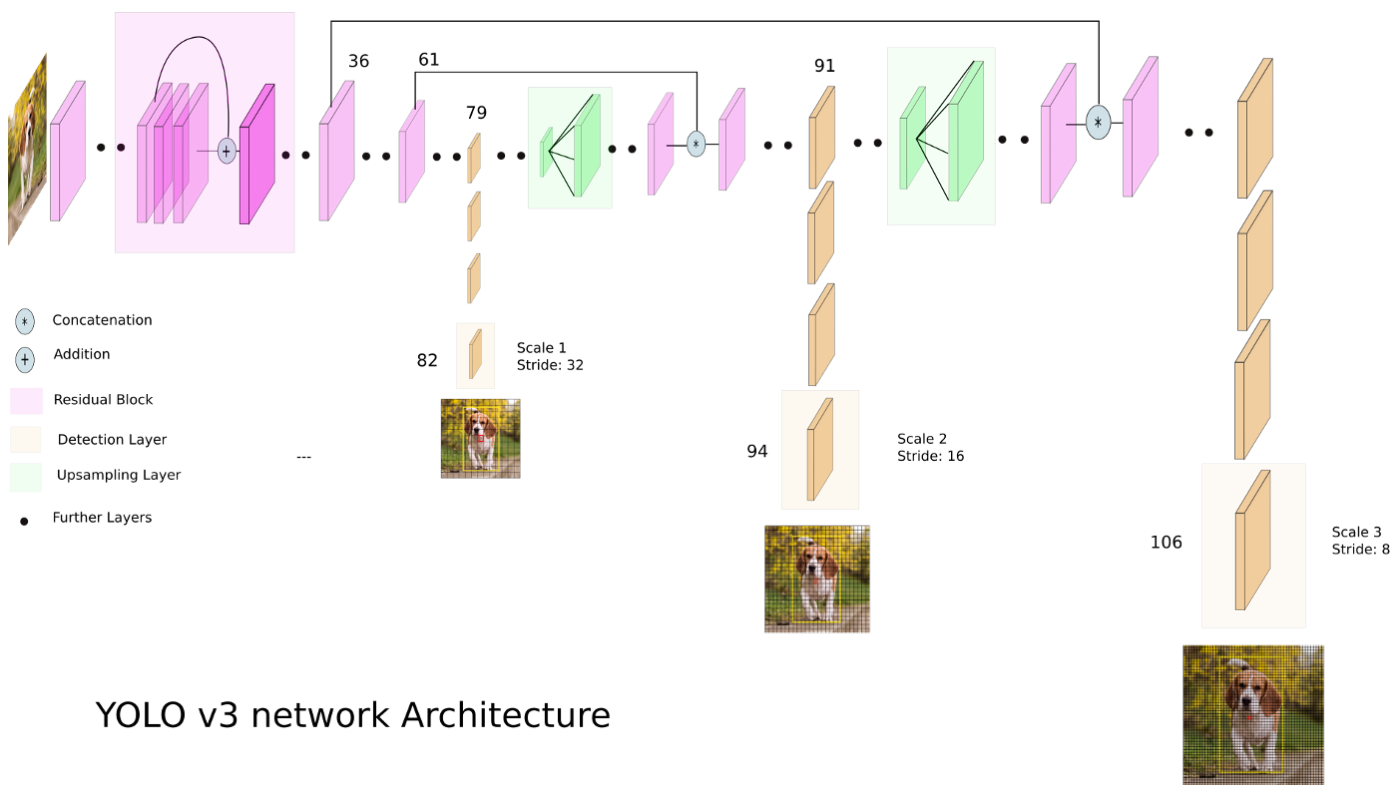


Figure 4.5: YOLO v3 network architecture

#### 4.2.2 Classification of delamination

It is observed from the radar images from the A1 projects that the delaminations, confirmed by the drill core samples, mainly show 3 types of structures, as indicated as follows:

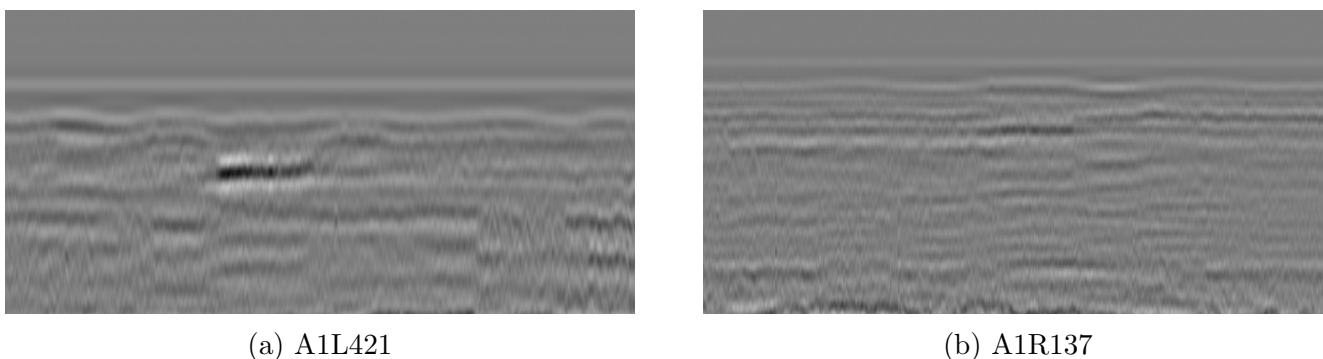


Figure 4.6: Examples of Type 1 delamination

Type 1 is the strong linear reflections, which often appear one by one and the amplitude overwhelms any other structure in the image, as shown in Figure 4.6a and 4.6b.

<sup>3</sup>The figure was created by Kathuria, in the passage 'What's new in YOLO v3?' published in Towards Data Science: <https://towardsdatascience.com/yolo-v3-object-detection-53fb7d3bfe6b>

The physical explanation is that the reflection of EM waves happens when the dielectric constant varies in the subsurface, and that such strong reflections correspond to sharp variation in material property. According to the default polarity in Examiner<sup>4</sup>, when the EM wave enters the subsurface from the air, the reflection pattern at the air-road surface interface shows the white color in the center part of the wavelet. When the EM wave enters a delamination that contains air in most space with little water from the asphalt, then the polarity reverses and thus the reflection pattern at the interface of such a delamination between asphalt layers shows the black color. Before these images are fed to the machine as training data, the whole strong reflection area is labeled.

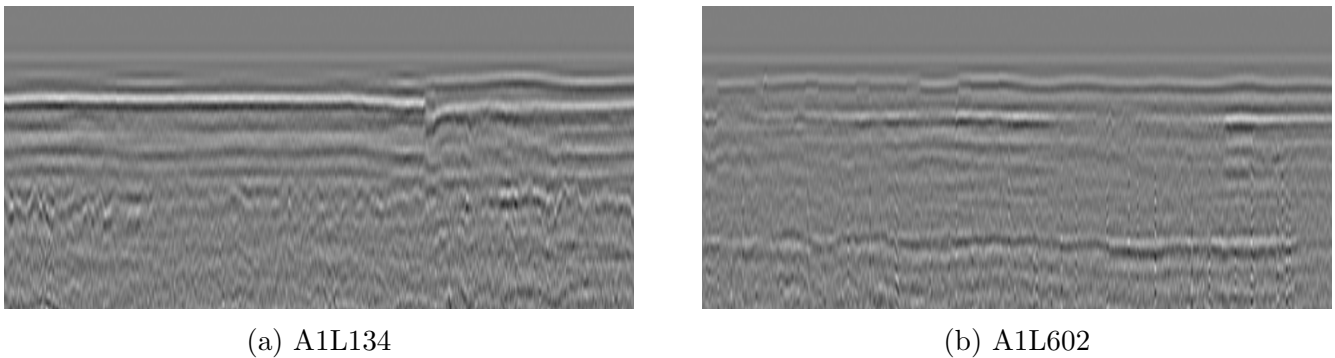


Figure 4.7: Examples of Type 2 delamination

Type 2 is featured by the appearance of truncation and/or loss, as shown in Figure 4.7a and 4.7b, corresponding to the discontinuity of a delamination which appear continually along the interface between asphalt layers, and only these structures are extracted during labelling.

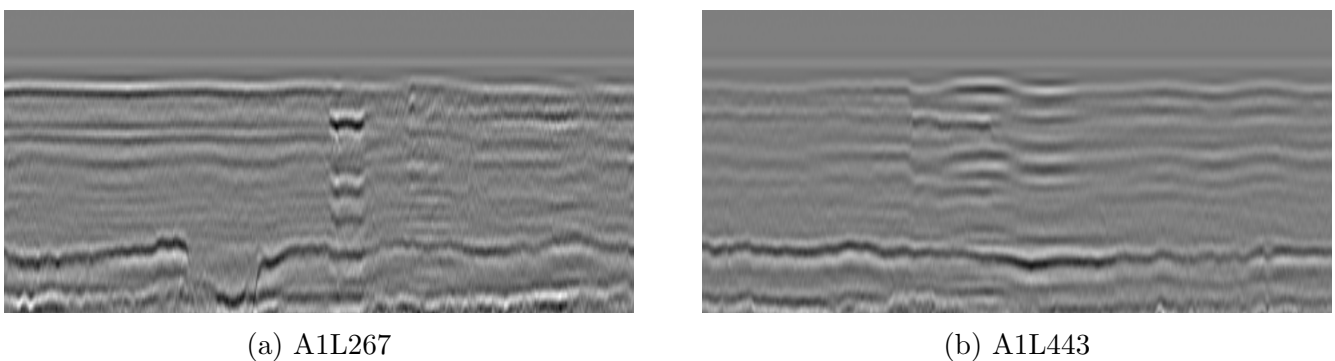


Figure 4.8: Examples of Type 3 delamination

Type 3 delamination is featured by multiple reflections, as shown in Figure 3.6 (a) and (b), and the whole structure of multiple reflections is extracted.

---

<sup>4</sup>There is an option that the polarity can be reversed, though this is usually not used in normal cases in road asphalt engineering.

One noticeable point is that structures with the aforementioned shapes are not necessarily real delaminations. This is absolutely true as the multiples reflections, for example, may not be delaminations but are ringing caused by some other factors like metal objects, and can also be caused by the strong variation of material properties. However, the logic behind the reasoning is that when given an image with a number of features which might be delaminations, the best thing for the machine to do is to detect everything that might be interesting. Even if it turns out that some of the detected structures are not delaminations, the amount of workload for human intervention can still be greatly reduced.

Thus, the false positives<sup>5</sup> in detection results are not a significant issue in this case, which could be accepted with some degree of tolerance, while the false negatives are, since asphalt engineers do not want existing delaminations to be neglected.

### 4.2.3 My datasets: training, validation and testing

As an application of the YOLO v3 algorithm, I trained the CNN with my own training and validation set and after that tested it with my testing set. Images with typical type(s) of delamination, with a total number of 108, were selected from the A1AT project<sup>6</sup>, with 40 images of Type 1 delamination, 34 images of Type 2 and 34 images of Type 3.

According to the a rule of thumb<sup>7</sup>, I selected 4 images out of the dataset of each type respectively as my testing set. Thus, my training and validation set contains 96 images altogether while 12 images are used as the first training set.

Moreover, I selected another 12 images from A1AT, out of the previously mentioned 108 images, each of which is either considered hard to classify, at least with human vision, or contains more than one delamination, and they composes the second training set.

In addition, the third training set consists of 12 images selected from the A1AA project. Thus, I have 3 testing sets in total, which were tested respectively as follows.

### 4.2.4 Testing results

After training, the performance of the algorithm on my first testing set is shown in Figure 4.9a - 4.9l, corresponding to each image in the testing set respectively. The green, red and blue boxes indicate the structures recognized as delamination of Type

---

<sup>5</sup>i.e. a structure which is actually not delamination is detected as delamination, while the false negatives are the opposite.

<sup>6</sup>One may be curious why the data sets are so small. However, the fact is that these are all that I can obtain at the moment. The explanation is shown in Appendix B.

<sup>7</sup>The ratio between training, validation and testing sets can be approximately around 8 : 1 : 1. Of course it's just a rule of thumb. For example, if in some case the ratio 7 : 1 : 2 is used, it is also fine. In my case, my training set together with validation set contains 96 images while the testing set has 12 images, and thus the ratio is something between the two mentioned ones.

1, 2 and 3 respectively, which is the same for detection results for all testing images from now on.

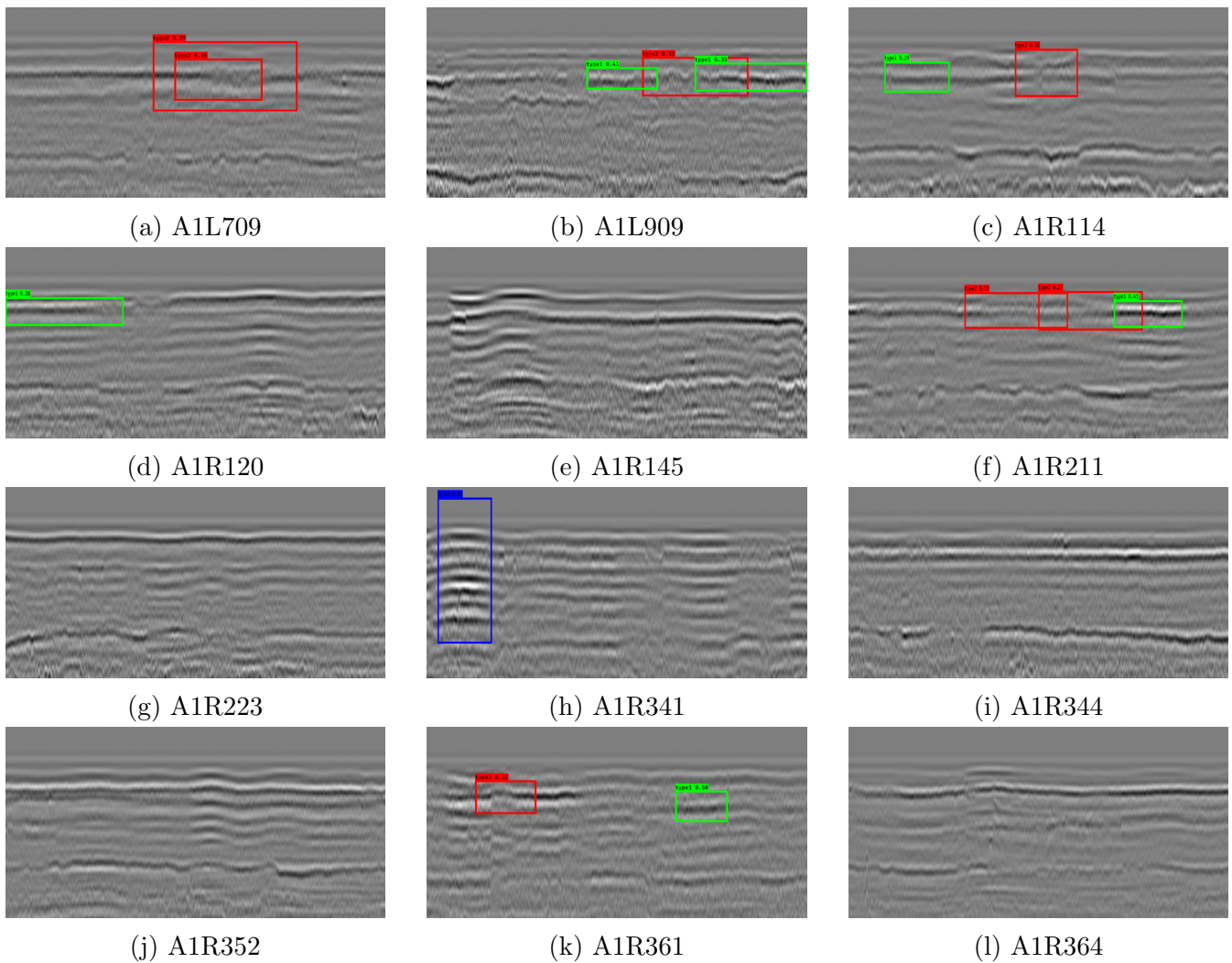


Figure 4.9: Results of detection on the testing set from A1AT (12 out of 108 images)

It is observed that 7 out of 12 images are detected with certain kind(s) of delamination, while no delamination is detected in the other 5 images.

Besides the number, some other aspects of performance are worth analysing. It is a good signal to observe that in the figures where at least one delamination was recognized, the most typical structures indicating the delaminations that I expected the machine to recognize were detected, indicating the effect of training. Although some redundancy also occurred, as is indicated in subfigure a as an example where the two red boxes actually detected the same featured structure, this is not a serious issue since asphalt engineers will not get confused when given detection result indicated by such a figure.

The fact that 5 figures which were not detected with any structures at all probably indicates that the training set is not sufficient in amount and/or not adequate enough in terms of image quality, and it may also indicate problem regarding the selection of area in the training images when they were being labeled.

When it comes to the second testing set, the performance of the algorithm is shown as follows in Figure 4.10a - 4.10l:

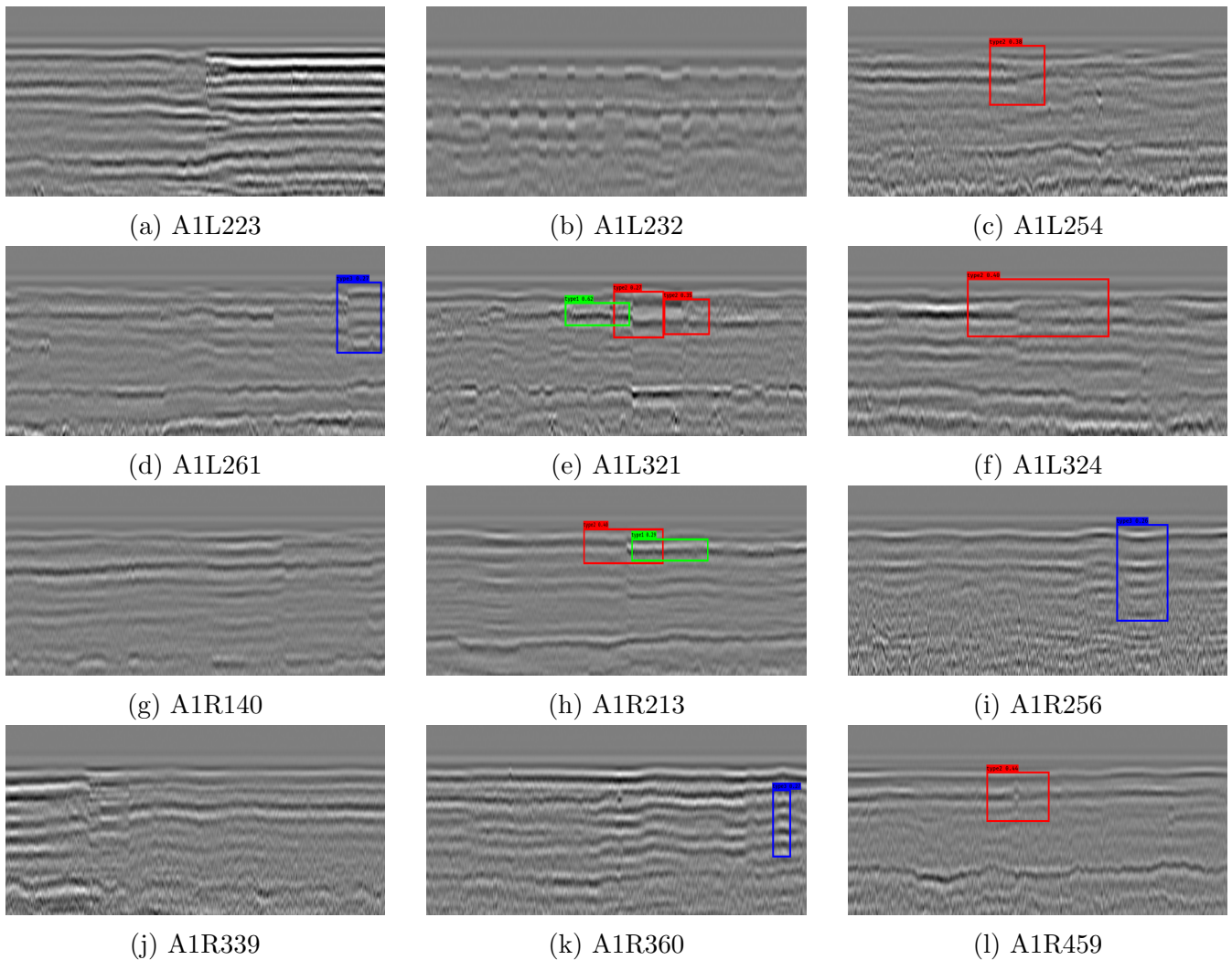


Figure 4.10: Results of detection on the testing set from A1AT (with more than one type)

As is shown above, among 12 images in the testing set, the features in 7 of them were detected as certain kind of delamination while no delamination was detected in the other 5 images.

Though some images in this testing set were considered as not that typical by human vision, for example subfigure (b), where a lot multiple reflections appear continually, which is abnormal and probably indicates certain kind of noise or measurement error, the general performance does not differ much from the first testing set.

In terms of amount of images detected, the performance on this testing set is even slightly better than that one the first one though this is not considered as a solid result in light of the size of training set.

Then the testing set is changed to 12 images from the A1AA project, and the results of detection on the third testing set are shown as follows in Figure 4.11a - 4.11l:

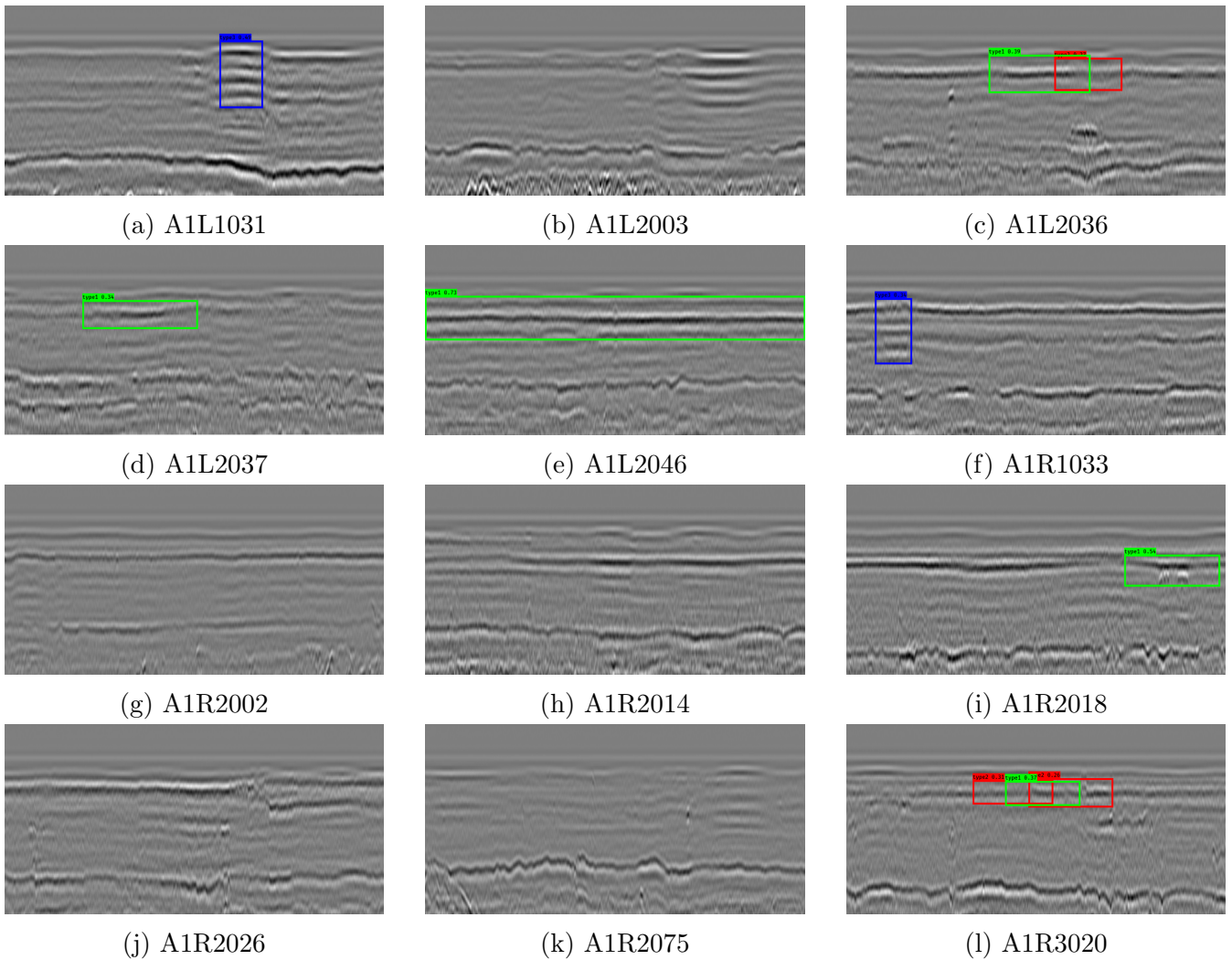


Figure 4.11: Results of detection on the testing set from A1AA

Again, the general performance is more or less the same, and the existing problems as indicated are also similar.

### 4.3 Summary and discussion

The EM algorithm, working for image segmentation, can separate the parts with interesting structures in a radar image with the rest, as the function of kind of 'rough indication', while it can hardly realize the specific target detection due to such way of working.

The delamination detection is realized, in this case, with an application of the YOLO v3 algorithm, though its performance on the testing sets indicates some possible existing problems, which need to be solved in the future given more available images for training.

The logic behind the reasoning and the inspiration are already clear: the false positives in detection results are not a significant issue in this case, but the false negatives are. If a decent extent of delamination detection, for example over 80%, is expected to be achieved, it will probably also mean a higher degree of tolerance of the false positives.

# Chapter 5

## Conclusions and future work

The functions and performance of the important inbuilt filters in Examiner were explored based on the acquired data. As an attempt to improve the visualization of cracks by filtering data principally, I obtained my own filters with a method based on a VNA-antenna-multilayered system model and our sky-shot and metal plate measurement data.

The checking results show that the solved filters do not show a satisfactory performance in either robustness or unbiasedness, and their magnitude patterns also differ from what was obtained in previous work.

However, this part of work has provided an application of the method based on the model has been constructed with the set of codes, as well as the points worth noticing and avoiding when making this application, including measurement details, data exporting, etc.. Accordingly, future work for this part may include:

1. To conduct new measurements that better satisfy the assumptions of the models and with higher measurement accuracy. For example, the heights were selected between 15 - 25 (cm) in this case since these are the heights that asphalt engineers most frequently used when setting a radar measurement. However, the results indicate that larger heights should probably be applied in future work to better satisfy the model assumptions.

2. Try to find some other way of data exporting from Examiner. In this case, we had no way to export the frequency domain data from Examiner directly and it turned out that the sampling frequency of the exported time domain data is not satisfactory enough. It will be beneficial to image data filtering if more satisfactory data can be exported with another way.

For the application of machine learning methods, the image segmentation was conducted by the EM algorithm, which highlights the interesting structures as kind of 'rough' recognition while the exclusive object detection was realized by an application of the YOLO v3 algorithm. The logic behind the reasoning is that the false positives in detection results are not the issue in this case, but the false negatives are. To achieve a decent extent of delamination detection will probably also mean a higher degree of acceptance of the false positives.

Its performance on the testing sets indicates some possible existing problems regarding training set, labelling, etc., which need to be solved in the future given more available images for training.

Sufficient size of training set is of great significance to ensure the performance of a CNN. In this project, I trained the CNN with my own training sets and tested its performance after that, based on all data I had at the moment. In light of the amount of data I had, I just put more efforts on the final performance of the trained CNN in this project, to get to know its performance on the given testing set at the moment, instead of the comparison and analysis parts of a machine learning task, such as visualize and analyze the training/validation loss and accuracy, calculating the performance on the testing set statistically, adjusting the training epoch, batch size, etc., to analyze their influence on the training as well as the final performance, since the current amount of data is too small to give solid and reliable results regarding the effect of training and performance.

However, this is a beginning and increasing amount of adequate radar data will be obtained in the future, not only with a larger amount but also with adequate image quality. Radar images with a high data quality is shown in Figure 5.1a and 5.1b as follows:

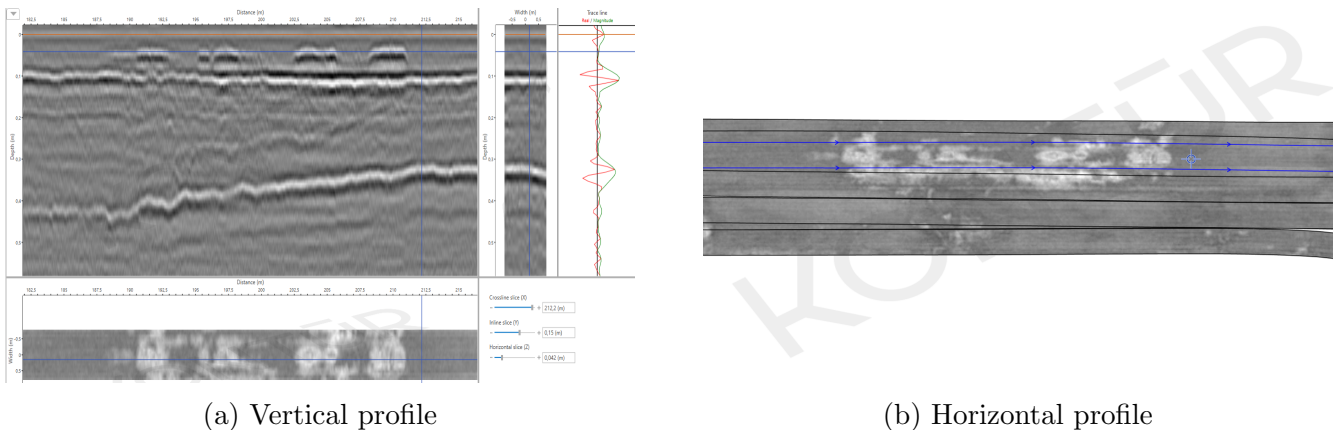


Figure 5.1: Examples of radar image from the demo project

These profiles are from a project for the purpose of demonstration (named as 'demo') provided by Kontur<sup>1</sup>. As is observed from the vertical profile, the delaminations in this demo project are clearly indicated by the reflection patterns. Of course images with such high quality can hardly be obtained in reality, but we should always try our best to improve radar data quality in future work, which will definitely be beneficial for further training of the CNN to get better results and can also be used for further analyses on the performance.

Moreover, if necessary, more types of variants of delaminations could be added into the category of delamination classification.

If better detection results for vertical radar profiles are obtained, we may even try to

<sup>1</sup>Official website of the company: <https://kontur.tech/>

apply the algorithm, for example, to a horizontal profile as shown in Figure 5.1b, or a video, etc., to detect damages within asphalt in a wider range of situations.

# Appendix A

## The Green's function of a metal plate

The Green's function corresponding to the electric field generated by an electric current source in space domain can be written as follows, according to eq.(38) in the paper by Hunziker et al. [4]:

$$G_{yy}^\uparrow(\vec{x}_r, \vec{x}_s, \omega) = -\frac{\zeta}{4\pi} \int_0^\infty \frac{\exp(-\bar{\Gamma}h)}{\bar{\Gamma}} J_0(k_\rho R) k_\rho dk_\rho + \frac{\partial_y \partial_y}{4\pi i \omega \epsilon_0} \int_0^\infty \frac{\exp(-\Gamma h)}{\Gamma} J_0(k_\rho R) k_\rho dk_\rho + \frac{\zeta \partial_y \partial_y}{4\pi i} \int_0^\infty \left( \frac{\exp(-\Gamma h)}{\Gamma} - \frac{\exp(-\bar{\Gamma}h)}{\bar{\Gamma}} \right) J_0(k_\rho R) k_\rho^{-1} dk_\rho \quad (\text{A.1})$$

where  $\zeta = i\omega\mu$ ,  $\Gamma = -ik_z = i\frac{\omega}{c_0}$ , and  $k_z^2 = k^2 - k_x^2 - k_y^2 = k^2 - k_\rho^2$ , while the physical meaning all the quantities involved are the same as what is stated in the 'Filters' chapter. In our case, there is no separation between the propagation directions of the EM wave, and thus we only use  $\Gamma$  without  $\bar{\Gamma}$ . Then the equation becomes:

$$G_{yy}^\uparrow(\vec{x}_r, \vec{x}_s, \omega) = \left( -\frac{i\omega\mu}{4\pi} + \frac{\partial_y \partial_y}{4\pi i \omega \epsilon_0} \right) \int_0^\infty \frac{\exp(ik_z h)}{-ik_z} J_0(k_\rho R) k_\rho dk_\rho \quad (\text{A.2})$$

According to the Sommerfeld identity [19][20], we have the relation:

$$\frac{\exp(ikR)}{R} = i \int_0^\infty dk_\rho \frac{k_\rho}{k_z} J_0(k_\rho R) \exp(ik_z h) \quad (\text{A.3})$$

Then the expression becomes:

$$G_{yy}^\uparrow(\vec{x}_r, \vec{x}_s, \omega) = \left( -\frac{i\omega\mu}{4\pi} + \frac{\partial_y \partial_y}{4\pi i \omega \epsilon_0} \right) \frac{\exp(ikR)}{R} \quad (\text{A.4})$$

With  $c_0 = \sqrt{\frac{1}{\epsilon_0 \mu_0}}$ , we get:

$$G_{yy}^\uparrow(\vec{x}_r, \vec{x}_s, \omega) = \left( \left( \frac{\omega}{c_0} \right)^2 + \partial_y \partial_y \right) \frac{\exp(-i\frac{\omega R}{c_0})}{4\pi i \omega \epsilon_0 R} \quad (\text{A.5})$$

To calculate the second term on the right-hand side (RHS), first calculate the first derivative:

$$\partial_y \frac{\exp(-i\frac{\omega R}{c_0})}{4\pi i\omega\epsilon_0 R} = \frac{\exp(-i\frac{\omega R}{c_0})(-i\frac{\omega}{c_0})\frac{\partial R}{\partial y} R - \exp(-i\frac{\omega R}{c_0})\frac{\partial R}{\partial y}}{R^2} \quad (\text{A.6})$$

In our case, the distance  $R$  is calculated as:

$$\begin{aligned} R(\vec{x}_r, \vec{x}_s, \omega) &= 2\sqrt{\left(\frac{\vec{x}_r - \vec{x}_s}{2}\right)^2 + \left(\frac{\vec{y}_r - \vec{y}_s}{2}\right)^2 + h^2} \\ &= \sqrt{(\vec{x}_r - \vec{x}_s)^2 + (\vec{y}_r - \vec{y}_s)^2 + 4h^2} \end{aligned} \quad (\text{A.7})$$

since the distance in a reflection in our case is the two way travelling distance. The derivative of distance  $R$  to the y-direction is:

$$\frac{\partial R}{\partial y} = \frac{y_r - y_s}{R} \quad (\text{A.8})$$

where the  $y_r, y_s$  here are scalars, indicating the offset between the receiver and source antennas. Put it into eq. (A.4), and then the first derivative is obtained:

$$\begin{aligned} \partial_y \frac{\exp(-i\frac{\omega R}{c_0})}{4\pi i\omega\epsilon_0 R} &= \frac{\exp(-i\frac{\omega R}{c_0})(-i\frac{\omega}{c_0})\frac{y_r - y_s}{R} R - \exp(-i\frac{\omega R}{c_0})\frac{y_r - y_s}{R}}{R^2} \\ &= \frac{\exp(-i\frac{\omega R}{c_0})}{R} \left( -i\frac{\omega}{c_0} \frac{y_r - y_s}{R} - \frac{y_r - y_s}{R^2} \right) \end{aligned} \quad (\text{A.9})$$

Then the second derivative:

$$\begin{aligned} \partial_y \partial_y \frac{\exp(-i\frac{\omega R}{c_0})}{4\pi i\omega\epsilon_0 R} &= \frac{\exp(-i\frac{\omega R}{c_0})}{R} \left( -\left(\frac{\omega}{c_0}\right)^2 \left(\frac{y_r - y_s}{R}\right)^2 + 3\left(\frac{y_r - y_s}{R^2}\right)^2 \right. \\ &\quad \left. + 3i\frac{\omega}{c_0} \frac{(y_r - y_s)^2}{R^3} + \left(-i\frac{\omega}{c_0} \frac{1}{R} - \frac{1}{R^2}\right) \right) \end{aligned} \quad (\text{A.10})$$

Since we assume that the offset between the source and receiver antennas only exists in the x-direction while there is no offset in the y-direction, i.e.  $x_r - x_s \neq 0$  while  $y_r - y_s = 0$ , the eq. (A.8) thus becomes:

Then the second derivative:

$$\partial_y \partial_y \frac{\exp(-i\frac{\omega R}{c_0})}{4\pi i\omega\epsilon_0 R} = \frac{\exp(-i\frac{\omega R}{c_0})}{R} \left( i\frac{\omega}{c_0} \frac{1}{R} - \frac{1}{R^2} \right) \quad (\text{A.11})$$

Thus, the Green's function of a metal plate is finally obtained:

$$\begin{aligned} G_{yy}^\uparrow(\vec{x}_r, \vec{x}_s, \omega) &= \frac{\exp(-i\frac{\omega R}{c_0})}{4\pi i\omega\epsilon_0 R} \left( \left(\frac{\omega}{c_0}\right)^2 + \partial_y \partial_y \right) \\ &= \frac{\exp(-i\frac{\omega R}{c_0})}{4\pi i\omega\epsilon_0 R} \left( \left(\frac{\omega}{c_0}\right)^2 - \left( i\frac{\omega}{c_0} \frac{1}{R} + \frac{1}{R^2} \right) \right) \end{aligned} \quad (\text{A.12})$$

# Appendix B

## Explanation on the choice of data set for object detection

The reasons contributing to the small data sets as mentioned are as follows:

First of all, only few among all road sections/sites measured contain 'remarkable' delaminations, i.e. more or less typical in pattern as what is discussed in the previous subsection. For example, patterns of some delaminations are so various and not typical that they are not close to the types as mentioned at all, and thus it is not suitable to feed them into the machine.

And when it comes to the radar images containing such delaminations with adequate image quality, the amount is even less. For example, in our case, the quality of the images from the A1AA project is generally much worse than that from the A1AT project, and this is exactly why images from my training sets were selected from A1AT while only 12 images with relatively adequate quality were chosen as one testing set from A1AA. Examples of radar images with high quality is shown in Figure 5.1a and 5.1b.

Moreover, only profiles with delaminations that were confirmed by drill core sample were taken to ensure the reliability of the results.

There are also no available historical data for this case, unfortunately, and thus I could only obtain all the images satisfying the aforementioned conditions one by one from Examiner.

# Bibliography

- [1] Sean Borman. The expectation maximization algorithm-a short tutorial. *Submitted for publication*, 41, 2004.
- [2] Chad Carson, Serge Belongie, Hayit Greenspan, and Jitendra Malik. Blobworld: Image segmentation using expectation-maximization and its application to image querying. *IEEE Transactions on pattern analysis and machine intelligence*, 24(8):1026–1038, 2002.
- [3] Frank Dellaert. The expectation maximization algorithm. Technical report, Georgia Institute of Technology, 2002.
- [4] Jürg Hunziker, Jan Thorbecke, and Evert Slob. The electromagnetic response in a layered vertical transverse isotropic medium: A new look at an old problem. *Geophysics*, 80(1):F1–F18, 2015.
- [5] Sébastien Lambot, EC Slob, I Van den Bosch, B Stockbroeckx, B Scheers, and Marnik Vanclooster. Gpr design and modeling for identifying the shallow subsurface dielectric properties. In *Proceedings of the 2nd International Workshop on Advanced Ground Penetrating Radar, 2003.*, pages 130–135. IEEE, 2003.
- [6] Sébastien Lambot, EC Slob, I Van Den Bosch, B Stockbroeckx, B Scheers, and Marnik Vanclooster. Estimating soil electric properties from monostatic ground-penetrating radar signal inversion in the frequency domain. *Water Resources Research*, 40(4), 2004.
- [7] Sébastien Lambot, Evert C Slob, Idesbald van den Bosch, Benoit Stockbroeckx, and Marnik Vanclooster. Modeling of ground-penetrating radar for accurate characterization of subsurface electric properties. *IEEE transactions on geoscience and remote sensing*, 42(11):2555–2568, 2004.
- [8] Bo Liu, Shengzheng Wang, Jiansen ZHAO, and Mingfeng LI. Ship tracking and recognition based on darknet network and yolov3 algorithm. *Journal of Computer Applications*, 39(6):1663, 2019.
- [9] KrishnanT McLachlanG. The em algorithm and extensions. whiley series in probability and statistics. *New York: JohnWiley&Sons*, 1997.

- [10] Thomas Minka. Expectation-maximization as lower bound maximization. *Tutorial published on the web at <http://www-white.media.mit.edu/tpminka/papers/em.html>*, 7:2, 1998.
- [11] Radford M Neal and Geoffrey E Hinton. A view of the em algorithm that justifies incremental, sparse, and other variants. In *Learning in graphical models*, pages 355–368. Springer, 1998.
- [12] Gilberto Ochoa-Ruiz, Andrés Alonso Angulo-Murillo, Alberto Ochoa-Zezzatti, Lina María Aguilar-Lobo, Juan Antonio Vega-Fernández, and Shailendra Natraj. An asphalt damage dataset and detection system based on retinanet for road conditions assessment. *Applied sciences*, 10(11):3974, 2020.
- [13] Debanjan Pathak and USN Raju. Content-based image retrieval using feature-fusion of groupnormalized-inception-darknet-53 features and handcraft features. *Optik*, 246:167754, 2021.
- [14] Joseph Redmon and Ali Farhadi. Yolo9000: better, faster, stronger. In *Proceedings of the IEEE conference on computer vision and pattern recognition*, pages 7263–7271, 2017.
- [15] Joseph Redmon and Ali Farhadi. Yolov3: An incremental improvement. *arXiv preprint arXiv:1804.02767*, 2018.
- [16] Enders A Robinson and Sven Treitel. *Geophysical signal analysis*. Society of Exploration Geophysicists, 2000.
- [17] Ashkan Sahari Moghaddam, Ehsan Rezazadeh Azar, Yolibeth Mejias, and Heather Bell. Estimating stripping of asphalt coating using k-means clustering and machine learning-based classification. *Journal of Computing in Civil Engineering*, 34(1):04019044, 2020.
- [18] Cedric Schmelzbach and Emanuel Huber. Efficient deconvolution of ground-penetrating radar data. *IEEE transactions on geoscience and remote sensing*, 53(9):5209–5217, 2015.
- [19] Arnold Sommerfeld. Über die ausbreitung der wellen inder drahtlosen telegraphie. 1909.
- [20] Arnold Sommerfeld. *Partial differential equations in physics*. Academic press, 1949.